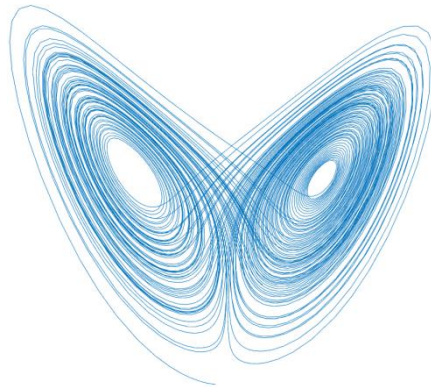


Institute of Physics Polish Academy of Sciences

PhD Thesis

**Investigation of the elastic
enhancement factor and $1/f^\alpha$ noise in
low-dimensional wave structures**

by
Vitalii Yunko



Supervisor: prof. dr hab. Leszek Sirko

Auxiliary supervisor: dr Michał Ławniczak

Warsaw 2018

ABSTRACT

The aim of this thesis is to present numerical and experimental studies of the elastic enhancement factor $W_{S,\beta}$ and the power spectrum $S(k)$, characterized by $1/f^\alpha$ noise dependence, in low-dimensional wave structures simulating quantum systems. For a completeness of the performed investigations, the short- and long-range correlations were also considered. The experimental studies have been conducted with the help of microwave networks and cavities which simulated quantum graphs and two-dimensional quantum billiards. Such simulations are possible due to a formal analogy between the Schrödinger equation that describes the motion of a particle in a graph and the Telegraph equation that describe the monochromatic wave propagating in a network. In the case of microwave cavities and quantum billiards the analogy holds due to the correspondence of the Helmholtz equation that describe the distribution of the electromagnetic field inside microwave resonators and the Schrödinger equation for particles in billiards.

The power spectrum $S(k)$ was also studied in three-dimensional (3D) microwave cavities. In this case the 3D Helmholtz equation is no longer equivalent to the 3D Schrödinger equation. However, it was shown that the properties of 3D chaotic microwave cavities can be modeled by the random matrix theory.

The studies of the elastic enhancement factor $W_{S,\beta}$ in rough and rectangular microwave cavities showed that $W_{S,\beta}$ can be used as a measure of system chaoticity. The elastic enhancement factor $W_{S,\beta}$ measured for a rectangular resonator displayed a transient behavior between integrable and chaotic systems. This behavior can be explained by the presence of microwave antennas used for the introduction and detection of microwave waves. The antennas behave as point-like perturbations which cause the deviations from the fully regular dynamics.

The power spectrum $S(k)$ of level fluctuations was investigated in microwave networks simulating quantum graphs with violated and preserved time reversal invariance. The obtained results indicate that the power spectrum $S(k)$ is highly sensitive to the number of missing levels. This property is extremely valuable in the experimental research where the identification of all levels is difficult or often impossible. Furthermore, the studies of the $S(k)$ distributions were also carried out for the rectangular and tree-dimensional microwave cavities. The obtained results were supplemented by the experimental and numerical evaluation of the short- and long-

range correlations related to energy level fluctuations such as the nearest-neighbor spacing distribution, the number variance, and the spectral rigidity. These functions together with the power spectrum $S(k)$ create an extremely useful tool for the determination of the number of missing levels.

STRESZCZENIE

W niniejszej rozprawie doktorskiej przedstawiono wyniki badań numerycznych i eksperymentalnych elastycznego współczynnika wzmocnienia $W_{S,\beta}$ oraz widma mocy $S(k)$, związanego z szumem $1/f^\alpha$, w niskowymiarowych strukturach mikrofalowych symulujących układy kwantowe. W badaniach uwzględniono korelacje krótkiego oraz dalekiego zasięgu. W doświadczeniach symulowano grafy i bilardy kwantowe za pomocą sieci oraz wnęk mikrofalowych. Symulacje te są możliwe dzięki formalnej analogii pomiędzy równaniem Schrödingera, opisującym ruch cząstki w grafie, a równaniem telegrafistów opisującym falę monochromatyczną propagującą się w sieci mikrofalowej. W przypadku dwuwymiarowych wnęk mikrofalowych i bilardów kwantowych podobna analogia występuje pomiędzy dwuwymiarowym równaniem Helmholtza opisującym rozkład pola elektromagnetycznego wewnątrz rezonatora a dwuwymiarowym równaniem Schrödingera dla cząstki w bilardzie.

Badania widma mocy $S(k)$ przeprowadzono także dla trójwymiarowych wnęk mikrofalowych. W tym przypadku trójwymiarowe równanie Helmholtza nie jest odpowiednikiem równania Schrödingera. Wykazano jednak, że właściwości chaotycznych trójwymiarowych wnęk mikrofalowych można modelować za pomocą teorii macierzy przypadkowych.

Badania współczynnika $W_{S,\beta}$ w chropowatych oraz prostokątnych wnękach mikrofalowych wykazały, że może on być dobrą miarą stopnia chaotyczności układu. Wyniki otrzymane dla rezonatora prostokątnego wykazały, że układ ten charakteryzuje się zachowaniem przejściowym między zachowaniem układu regularnego i chaotycznego. Takie właściwości układu można wytłumaczyć obecnością anten używanych do wprowadzenia oraz detekcji fal mikrofalowych. Anteny takie zachowują się tak jak punktowe rozpraszacze, co powoduje iż układ ten przestaje być w pełni regularnym.

Widmo mocy $S(k)$ zbadano dla sieci mikrofalowych symulujących zarówno grafy kwantowe ze złamaną jak i z zachowaną symetrią ze względu na odwrócenie czasu. Otrzymane rezultaty wykazały dużą wrażliwość widma mocy $S(k)$ na liczbę zgubionych poziomów energetycznych. Wynik ten jest niezwykle cenny w badaniach eksperymentalnych, gdzie zidentyfikowanie wszystkich poziomów jest trudne, a często niemożliwe. Badania rozkładów widma mocy $S(k)$ przeprowadzono także dla

prostokątnych i trójwymiarowych wnęk rezonansowych. Otrzymane wyniki zostały uzupełnione dodatkowymi badaniami krótko i dalekozasięgowych funkcji korelacji związanych z fluktuacjami poziomów energetycznych, takimi jak: rozkład odległości sąsiednich poziomów energetycznych, wariancja poziomów oraz sztywność spektralna. Funkcje te, wraz z widmem mocy $S(k)$, stanowią niezwykle użyteczne narzędzie, które z sukcesem może być stosowane do wyznaczania liczby zgubionych poziomów energetycznych.

LIST OF PUBLICATIONS

- Michał Ławniczak, Małgorzata Białous, Vitalii Yunko, Szymon Bauch, and Leszek Sirko, “*Experimental investigation of the elastic enhancement factor in a transient region between regular and chaotic dynamics*”, Phys. Rev. E **91**, 032925 (2015).
- Michał Ławniczak, Małgorzata Białous, Vitalii Yunko, Szymon Bauch, and Leszek Sirko, “*Numerical and experimental studies of the elastic enhancement factor for 2D open systems*”, Acta Physica Polonica A **128**, 974 (2015).
- Małgorzata Białous, Vitalii Yunko, Szymon Bauch, Michał Ławniczak, Barbara Dietz, and Leszek Sirko, “*Power spectrum analysis and missing level statistics of microwave graphs with violated time reversal invariance*” Phys. Rev. Lett. **117**, 144101 (2016).
- Małgorzata Białous, Vitalii Yunko, Szymon Bauch, Michał Ławniczak, Barbara Dietz, and Leszek Sirko, “*Long-range correlations in rectangular cavities containing point-like perturbations*” Phys. Rev. E **94**, 042211 (2016).
- Barbara Dietz, Vitalii Yunko, Małgorzata Białous, Szymon Bauch, Michał Ławniczak, and Leszek Sirko, “*Nonuniversality in the spectral properties of time-reversal-invariant microwave networks and quantum graphs*”, Phys. Rev. E **95**, 052202 (2017).
- Michał Ławniczak, Małgorzata Białous, Vitalii Yunko, Szymon Bauch, Barbara Dietz and Leszek Sirko, “*Analysis of missing level statistics for microwave networks simulating quantum chaotic graphs without time reversal symmetry — the case of randomly lost resonances*”, Acta Physica Polonica A **132**, 1672 (2017).
- Michał Ławniczak, Małgorzata Białous, Vitalii Yunko, Szymon Bauch, and Leszek Sirko, “*Missing-level statistics and analysis of the power spectrum of level fluctuations of three-dimensional chaotic microwave cavities*”, Phys. Rev. E **98**, 012206 (2018).

- Vitalii Yunko, Małgorzata Białous, Szymon Bauch, Michał Ławniczak, and Leszek Sirko “*Experimental and numerical study of spectral properties of three-dimensional chaotic microwave cavities: The case of missing levels*” The 11th CHAOS 2018 International Conference (2018), to be printed.

CONTENTS

1. INTRODUCTION.....	11
1.1. Motivation.....	11
1.2. Birth of chaos studies.....	12
1.3. Chaotic dynamics.....	13
2. TIME REVERSAL SYMMETRIES AND RANDOM MARIX THEORY.....	15
2.1. Time reversal symmetry.....	15
2.2. Gaussian ensembles in random matrix theory.....	16
2.2.1. Gaussian Orthogonal Ensemble (GOE).....	17
2.2.2. Gaussian Symplectic Ensemble (GSE).....	17
2.2.3. Gaussian Unitary Ensemble (GUE).....	18
2.3. The nearest neighbor spacing distributions (NNSD) and unfolding of the spectrum.....	18
3. WAVE CHAOS.....	21
3.1. Quantum graphs.....	21
3.2. Microwave networks.....	23
3.3. Quantum billiards.....	26
3.4. Microwave cavities.....	28
4. LONG-RANGE CORRELATIONS AND THE ELASTIC ENHANCEMET FACTOR.....	31
4.1. Number variance and Dyson-Mehta statistic.....	31
4.2. $1/f^\alpha$ noise.....	33
4.3. The elastic enhancement factor.....	35
5. MISING LEVELS IN SPECTRAL FLUCTUATION.....	38
6. THE ELASTIC ENHANCEMENT FACTOR AS A MEASURE OF INTERNAL CHAOS.....	41
7. MISSING LEVEL STATISTICS IN MICROWAVE NETWORKS.....	50
7.1. Missing level statistics of microwave networks with broken TRS.....	50
7.2. Missing level statistics of microwave networks with preserved TRS.....	58
8. MISSING-LEVEL STATISTICS OF THE THREE-DIMENSIONAL CHAOTIC MICROWAVE CAVITIES.....	63
9. CONCLUSIONS.....	73
BIBLIOGRAPHY.....	75

CHAPTER 1

INTRODUCTION

1.1. Motivation

The main objective of this thesis is the experimental and numerical study of properties of low-dimensional wave structures simulating quantum systems by investigating the elastic enhancement factor $W_{S,\beta}$ and the power spectrum $S(k)$, characterized by $1/f^\alpha$ noise dependence. These investigations are in the most cases linked with chaotic behavior of the studied systems. In mass culture chaos is very often associated with disorder but this interpretation is misleading. Classically chaos is a result of a nonlinear dependence of a system evolution, described by a shape of an trajectory in a phase space, on its initial conditions. In other words, chaos theory is focused on the behavior of dynamical systems that are highly sensitive to the initial conditions. It is widely applicable to a variety of situations. Some areas benefiting from chaos theory are e.g., geology, mathematics, microbiology, biology, meteorology, philosophy, computer science, economics, engineering, algorithmic trading, physics, psychology, and robotics [1-3].

Unfortunately, due to the Heisenberg uncertainty principle, the notion of well defined trajectories in the phase space can't be applied to quantum systems. The following question arises whether we are able to verify and describe the chaotic nature of the quantum system. Indeed, it is possible by investigating spectral properties of quantum systems whose classical counterparts are chaotic. For this purpose, we used the models of quantum graphs and billiards that are microwave networks and cavities, respectively. It is possible due to the formal analogy between the Schrödinger equation, describing quantum systems, and the Telegraph and the two-dimensional Helmholtz equations, describing microwave networks and cavities, respectively.

Despite of a continuous increase of the interest in quantum chaos, studies performed so far are focused mostly on theoretical problems while the experimental studies are still very scarce. Experimental research is especially important for complicated, interacting with the environment systems. The significance of such

investigations is difficult to overestimate. For example, it was shown in 2012 that two geometrically different microwave networks, simulating quantum graphs, have the same amplitudes and phases of the determinants of the scattering matrices [4], therefore, they are isoscattering.

As it will be demonstrated in this thesis, the elastic enhancement factor and the power spectrum that exhibits the power law behavior characterized by $1/f^\alpha$ noise, are the perfect measures for investigation of the quantum systems which classical counterparts are chaotic or partly chaotic. With their help it is possible not only to determine the degree of chaoticity of a studied quantum system but also to attribute it to the corresponding symmetry class. It is not even necessary to emphasize how important it is to know whether a studied system exhibits chaotic behavior or not.

I sincerely hope that presented work will contribute to an area of quantum chaos studies and non-linear physics, and that it covered important aspects of experimental investigations which have not been studied yet.

1.2. Birth of chaos studies

From the beginning of time people were trying to explain different phenomena that surrounded them. Various mathematical models were implemented to describe physical properties of the investigated systems.

Birth of chaos theory very often is related with studies of Henri Poincaré. In his research on the three-body problem, Poincaré noticed chaotic behavior in deterministic system. In particular, he found that a small perturbation of the initial state, namely body position, leads to a totally different later state in comparison with the unperturbed one. Unfortunately, his works weren't recognized among scientific society. Nevertheless, inspired by Poincaré's results, Russian scientist Andrei Kolmogorov showed [5] further that a quasiperiodic regular motion can persist in an integrable system due to small perturbations.

Yet official discoverer of the chaos theory is Edward Lorenz. The first observation of phenomena which later will be called chaos theory is dated 1963 [6]. Lorenz calculations with uncontrolled approximations for weather predictions surprisingly did not match after each repetition of same procedure. The assumption that minor changes in the initial condition will lead to changes in conclusive results of the

same magnitude wasn't true in this case. Lorenz also presented a graphical representation of his findings, achieved figure was nothing else but the attractor.

Even though studies in this direction have already been carried out, officially term chaos was coined by James A. Yorke and T.Y. Li in 1975 [7].

1.3. Chaotic dynamics

In classical Hamiltonian mechanics there are two radically different types of motion: the regular one of integrable systems and the chaotic motion of nonintegrable systems. In order to identify the type of motion for a given dynamical system one may analyze a pack of trajectories originating from a small area of points in the phase space.

A very often used measure of classical chaos in a dynamical system is the Lyapunov exponent which characterizes the rate of separation of infinitesimally close trajectories. Quantitatively, two trajectories in phase space with the initial separation $\Delta a_{12}(0)$ (Fig. 1.1) diverge at a rate given by

$$|\Delta a_{12}(t)| = e^{\lambda t} |\Delta a_{12}(0)|, \quad (1.1)$$

where λ is the Lyapunov exponent.

A negative Lyapunov exponent ($\lambda < 0$) is characteristic of dissipative or non-conservative systems [8]. A system exhibits steady state mode when $\lambda = 0$. When the value of λ is positive, it's a sign of unstable and chaotic trajectories. It works for discrete as well as continuous systems.

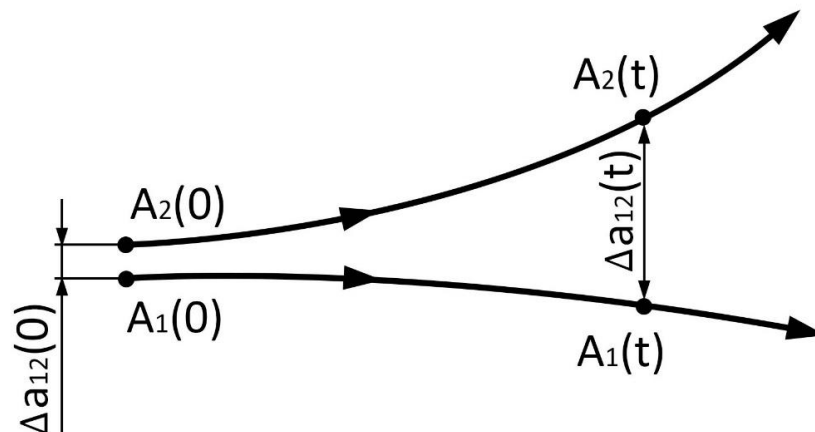


Fig. 1.1: Separation of two trajectories A_1 and A_2 in phase space in a function of time t .

The multiplicative inverse of the largest Lyapunov exponent is sometimes referred as the Lyapunov time. This characteristic goes further than determination of the dynamics of a given system, also providing limits of the predictability of the system. For chaotic trajectories, the Lyapunov time is finite and can take varied values, like 5 million years for Solar system or 2 seconds for hydrodynamic chaotic oscillations. In the case of regular trajectories, the Lyapunov time will take the value of infinity.

It's completely another story when quantum effects are considered, as due to Heisenberg uncertainty principle, this criterion can't be applied to quantum systems. The notion of a phase space trajectory loses its meaning, as a result the Lyapunov exponent loses its usefulness. Nevertheless, other quantum mechanical criteria, which can be used for distinguishing between different type of quantum dynamics, do exist, and they are used by scientist for a few decades already. Some are based on properties of short- and long-range spectral correlation functions and some on properties of scattering matrices.

CHAPTER 2

TIME REVERSAL SYMMETRIES AND RANDOM MARIX THEORY

2.1. Time reversal symmetry

The solution $\psi(x, t)$ of the Schrödinger equation

$$i\hbar \dot{\psi}(x, t) = H \psi(x, t), \quad (2.1)$$

is time-reversal if there is another solution $\psi'(x, t')$ with $t' = -t$ and ψ' is uniquely related to ψ [9].

For particles without spin the time reversal operator $T = K$, where K is the operator of complex conjugation. The transformation of a wave function does not change the modulus of the overlap of two wave functions,

$$|\langle K\psi | K\varphi \rangle|^2 = |\langle \psi | \varphi \rangle|^2, \quad (2.2)$$

while the overlap itself is transformed into its complex conjugate,

$$\langle K\psi | K\varphi \rangle = \langle \psi | \varphi \rangle^* = \langle \varphi | \psi \rangle. \quad (2.3)$$

More general form of time reversal operator, applicable also to particles with spin, is given by

$$T = UK, \quad (2.4)$$

where U is an unitary operator.

When the wave function is acted upon twice by T it should be reproduced to fulfill requirement of time-reversal operator

$$T^2 = \pm 1. \quad (2.5)$$

The negative sign holds in the case of the spin $\frac{1}{2}$, while the positive sign remains for the spinless particles. In order to keep time reversal symmetry and to introduce the spin, the relation

$$TJT^{-1} = -J, \quad (2.6)$$

needs to be hold both for an angular momentum and the spin. The operators associated with the spin $\frac{1}{2}$ are

$$\hat{S} = \frac{\hbar}{2} \hat{\sigma}, \quad (2.7)$$

where $\hat{\sigma}$ denote Pauli matrices

$$\sigma_x = \begin{pmatrix} 0 & 1 \\ 1 & 0 \end{pmatrix}, \quad \sigma_y = \begin{pmatrix} 0 & -i \\ i & 0 \end{pmatrix}, \quad \sigma_z = \begin{pmatrix} 1 & 0 \\ 0 & -1 \end{pmatrix}. \quad (2.8)$$

In the case of operators squating to minus unity $T^2 = -1$, all eigenvalues of Hamiltonian exhibit Kramer's degeneracy - for every energy eigenstate of a system with half-integer total spin and preserved time-reversal symmetry, there is at least one more eigenstate with the same energy.

Hamiltonians without T invariance, unrestricted by antiunitary symmetries, are constituted by unitary matrices.

2.2. Gaussian ensembles in random matrix theory

A mathematical model named random matrix theory (RMT) originates from nuclear physics, particularly from the study of nuclear reactions of average behavior of the various energy levels. Complicated many-body interactions naturally give rise to the statistical theories, one of which is RMT. Random matrix theory handles Hamiltonians (H) by representing them with Hermitian matrices. Such an approach has arisen due to the fact that very often we do not know H , or it's too complex to be solved, but it's still possible to make statistical hypotheses on Hamiltonian, compatible with the general symmetry properties. Generally, except of a few untypical cases, all those Hamiltonian matrices will give same spectral fluctuation depending on their group of canonical transformation. Matrix elements are random variables, and their statistical independence is limited to requirements of corresponding symmetry. The most studied random matrices are the Gaussian ensembles. Performing a group-theoretical analysis, Dyson discovered that an irreducible ensemble of matrices, invariant under symmetry group, unquestionably belongs to one of three classes. Considered by him classes obtained the following names: orthogonal, unitary, and symplectic [10].

2.2.1. Gaussian Orthogonal Ensemble (GOE)

The GOE models even-spin systems which are invariant under time-reversal. In this case, every such a system with preserved time reversal symmetry, will be associated with a real symmetric matrix H . The representation of states needs to be suitably chosen [10]. Two requirements define the Gaussian Orthogonal Ensemble in the space of real symmetric matrices. First, its distribution should be invariant under real orthogonal transformation

$$H_{mj} = H_{jm}. \quad (2.9)$$

Second, the various elements $H_{mj}, m \leq j$ should be statistically independent.

Probability density function $P(H)dH$ that a system will belong to the volume element $dH = \prod_{m \leq j} dH_{mj}$, could be written as follows

$$P(H) = \prod_{m \leq j} f_{mj}(H_{mj}). \quad (2.10)$$

2.2.2. Gaussian Symplectic Ensemble (GSE)

The GSE models Hamiltonians for odd-spin systems with time-reversal symmetry but no rotational symmetry. The Hamiltonian matrix of GSE can be written in terms of Pauli spin matrices [11]

$$H_{mj} = H_{jm}^{(0)} I_2 - i \sum_{\lambda=1}^3 H_{jm}^{(\lambda)} \sigma_{\lambda}, \quad (2.11)$$

where I_2 – identity matrix of size 2, σ_{λ} – Pauli spin matrices, $H_{jm}^{(0)}$ – real symmetric matrix and $H_{jm}^{(1)}, H_{jm}^{(2)}, H_{jm}^{(3)}$ – real antisymmetric matrices.

The probability $P(H)dH$ where the volume element equals to

$$dH \equiv \prod_{m \leq j} dH_{mj}^{(0)} \prod_{\lambda=1}^3 \prod_{m < j} dH_{mj}^{(\lambda)}, \quad (2.12)$$

is a product of functions each of which depends on a single variable

$$P(H) = \prod_{m \leq j} f_{mj}^{(0)}(H_{mj}^{(0)}) \prod_{\lambda=1}^3 \prod_{m < j} f_{mj}^{(\lambda)}(H_{mj}^{(\lambda)}). \quad (2.13)$$

2.2.3. Gaussian Unitary Ensemble (GUE)

The GUE models Hamiltonians with violated time-reversal symmetry. Arbitrary Hermitian matrices that are not restricted to be real or self-dual are used to represent Hamiltonian of a system without time-reversal invariance.

$$H_{mj} = H_{jm}^*. \quad (2.14)$$

The probability $P(H)dH$ that system will belong to the volume element

$$dH = \prod_{m \leq j} dH_{mj}^{(0)} \prod_{m < j} dH_{mj}^{(1)}, \quad (2.15)$$

is invariant under every automorphism and equals to

$$P(H) = \prod_{m \leq j} f_{mj}^{(0)}(H_{mj}^{(0)}) \prod_{m < j} f_{mj}^{(1)}(H_{mj}^{(1)}), \quad (2.16)$$

where $H_{mj}^{(0)}$ and $H_{mj}^{(1)}$ are real and imaginary parts of H_{mj} .

$P(H)$ can be written without loss of generality for all three cases as follows [9]

$$P(H) = C e^{-A \text{Tr} \{H^2\}}. \quad (2.17)$$

A is a constant that fixes unit of energy and C is determined by the normalization. By considering symmetry class ($\beta = 1, 2, 4$ for GOE, GUE and GSE, respectively) and matrices size (N), the above formula can be written [12]

$$P_{\beta N}(H) \approx \left(\frac{A}{\pi}\right)^{\frac{N}{2}} \left(\frac{2A}{\pi}\right)^{\frac{N(N-1)\beta}{2}} e^{-A \text{Tr} \{H^2\}}. \quad (2.18)$$

2.3. The nearest neighbor spacing distributions (NNSD) and unfolding of the spectrum

A short-range correlation function NNSD (the nearest neighbor spacing distribution) is the most frequently used spectral statistics which can probe chaotic properties of quantum systems. The NNSD is the probability of finding two neighboring energy levels with the specified distance between them. The NNSD shows that non-degenerated states prevail in chaotic systems. This phenomenon is called the level repulsion and is a characteristic feature of quantum chaotic systems.

Joint distribution of eigenenergies E_μ is [9]

$$P(E) = \text{const} \prod_{\mu < \nu}^{1..N} |E_\mu - E_\nu|^\beta e^{-A \sum_{\mu=1}^N E_\mu^2}. \quad (2.19)$$

From the sequence of eigenenergies one defines the normalized spacings

$$s_\mu = \frac{(E_{\mu+1} - E_\mu)}{\langle s \rangle}. \quad (2.20)$$

The NNSD for presented in the previous section random matrix statistics is approximately given in GOE by

$$P(s) = \frac{s\pi}{2} e^{-s^2 \frac{\pi}{4}}, \quad (2.21)$$

in GSE by

$$P(s) = \frac{s^4 2^{18}}{3^6 \pi^3} e^{-s^2 \frac{64}{9\pi}}, \quad (2.22)$$

and finally in GUE by

$$P(s) = \frac{s^2 32}{\pi^2} e^{-s^2 \frac{4}{\pi}}. \quad (2.23)$$

If underlying dynamics is regular, the energy levels will behave like independent random variables from a Poisson process [13]. In general, Poisson distribution is a discrete probability distribution that expresses the probability of a given number of events (in case of NNSD spacing between neighboring levels), occurring in a fixed interval of time or space. These events should occur with a known constant rate and independently of the time since the last event. The nearest-neighbor spacing distribution has in this case a simple form

$$P(s) = e^{-s}. \quad (2.24)$$

Another important short-range spectrum fluctuation measure is the integrated NNSD, $I(s)$, which exploits dependence at small level separations s

$$I(s) = \int_0^s ds' P(s'). \quad (2.25)$$

The expected degree of level repulsion for all random matrix ensembles and the Poisson random process is illustrated in Fig. 2.1.

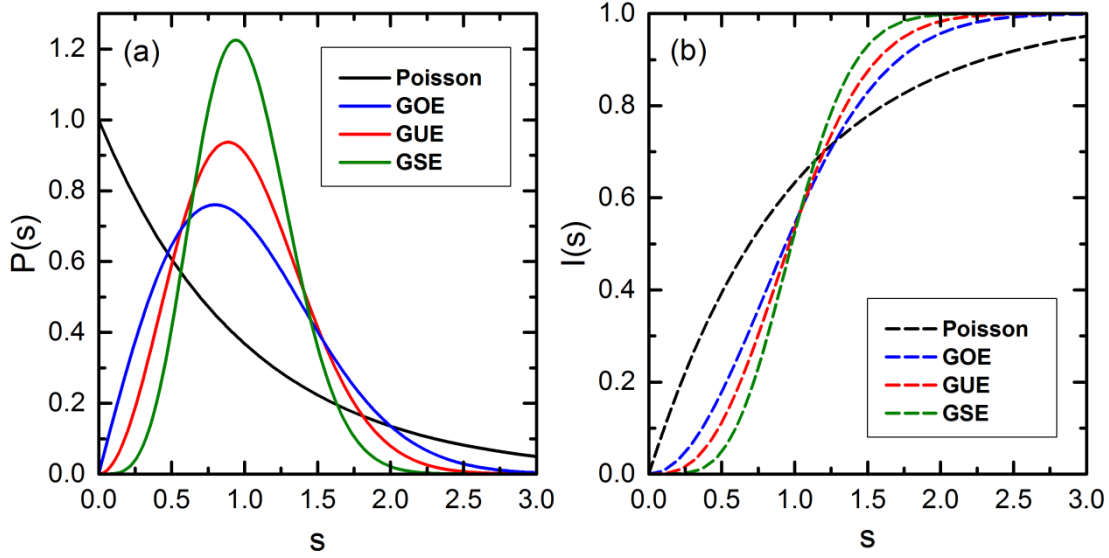


Fig. 2.1: (a) The NNSD for the Gaussian ensembles and the Poisson random process. (b) The integrated NNSD for the Gaussian ensembles and the integrated Poisson random process.

A given sequence of measured or calculated levels usually contains system specific properties. To separate the local level density from the overall energy dependence of the level separation, a procedure of unfolding needs to be performed. It is usually done by calculating staircase function of the observed spectra, which is the number of levels ΔN below or at the energy E [14]. The rescaled levels should have the unit mean spacing, whereas the mean should be evaluated with respect to the energy intervals. The average level staircase has the form [9]

$$\bar{f}(E) = \int_{-\infty}^E dE' \rho(E'), \quad (2.26)$$

where $\rho(E)$ is mean level density.

The unfolded spectrum is formed by dimensionless variables

$$\epsilon_i = \bar{f}(E_i). \quad (2.27)$$

CHAPTER 3

WAVE CHAOS

Quantum chaos was essentially a domain of theory, and to some extent this pattern has been preserved. However, there are also studies that can be beneficial in practice, for example: controlling chaos in the vibronic lasers [15], and passively modelocked Ti:Sapphire oscillator [16], etc. The pioneering works, based on experimental approach, are devoted to the properties of spectra of compound nucleus, highly excited hydrogen and alkali atoms [17]. The recent directions in quantum chaos concern both universal and non-universal features of eigenenergies and eigenfunctions of quantum systems, whose classical counterparts display chaotic behaviors. Microwave networks [18, 19] and microwave resonators [20, 21] simulating quantum graphs and billiards are very often used to perform such kind of research. Properties of the microwave networks and quantum graphs depend very sensitively on their structure, while those of the microwave and quantum billiards depend on the shapes of the systems. Classical analogues of quantum systems can exhibit chaotic, regular or mixed dynamics. Despite of many theoretical studies, there are some features in the spectra of real physical systems that are not yet fully understood. Conducted by me research aimed at investigation of such theoretical problems using an experimental model systems such as microwave networks and billiards.

3.1. Quantum graphs

A quantum graph was introduced by Linus Pauling as a model of free electrons in organic molecules [22]. This simple model arises in a variety of mathematical and physical contexts, for instance, in simulation of quantum wires [23], optical waveguides [24] and mesoscopic quantum systems [25, 26]. Moreover, it was used to study quantum chaos [4, 18, 27-29].

A metric graph is a graph which consist of a set b of vertices and a set e of edges (or bonds). The valency b_i of a vertex b is the number of edges meeting at that vertex. If all edges always join pairs of vertices, such graph is called combinatorial graph.

If at least one edge attached to a single vertex is semi-infinite then such a graph is called open. The graph is called b -regular if all the vertices have the same valency. Each graph can be characterized by a square connectivity matrix $C_{i,j} = C_{j,i}$ of size b [30].

$$C_{i,j} = C_{j,i} = \begin{cases} 1 & \text{if } i,j \text{ are connected} \\ 0 & \text{otherwise} \end{cases} \quad (3.1)$$

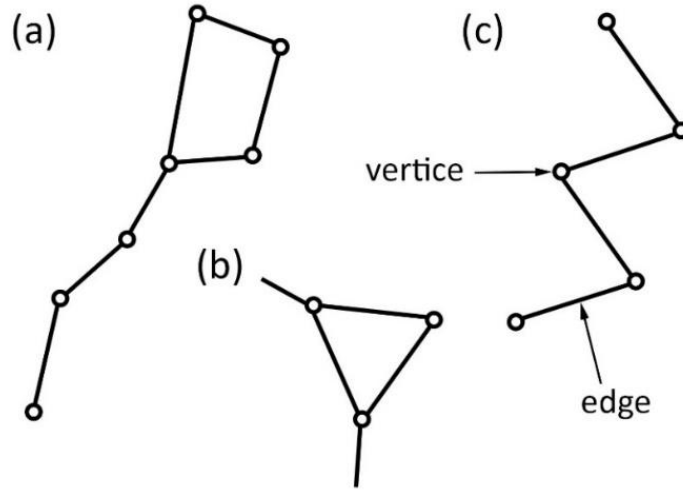


*Fig. 3.1: Graphs examples: (a) a combinatorial graph with $e=7$ and $b=7$;
(b) an open graph that possesses two open edges with total $e=5$ and $b=3$;
(c) a combinatorial graph with $e=4$ $b=5$.*

Each edge is specified with a positive length interval $[0, L_e]$, where the position coordinate for one of the connected vertices $x_e = 0$ and $x_e = L_e$ for another. In the case of semi-infinite edge $L_e = \infty$.

Quantum graphs are metric graphs with a differential operator acting on functions defined on the edges. On each edge e , the component Ψ_e of the total wavefunction Ψ is a solution of the one-dimensional equation ($\hbar = 2m = 1$) [30]

$$\left(-i \frac{d}{dx^2} - A_e\right)^2 \Psi_e(x) = k^2 \Psi_e(x), \quad (3.2)$$

where A_e is a magnetic vector potential responsible for breaking of time reversal symmetry.

For the systems with time reversal symmetry $A_e = 0$. The vertex matching conditions (Neumann conditions) comprise that $\Psi_e(x)$ is continuous, that means the values at the vertex agree among all functions acting on the edges attached to the vertex

$$\Psi_{i,j}(x)|_{x=0} = \varphi_i, \quad \Psi_{i,j}(x)|_{x=L_e} = \varphi_j \quad \text{for all } i < j \text{ and } C_{i,j} \neq 0. \quad (3.3)$$

The second condition has the form [31]

$$\sum_{j < i} C_{i,j} \left(iA_{j,i} - \frac{d}{dx} \right) \Psi_{j,i}(x) \Big|_{x=L_e} + \sum_{j > i} C_{i,j} \left(-iA_{i,j} + \frac{d}{dx} \right) \Psi_{i,j}(x) \Big|_{x=0} = \lambda_i \varphi_i, \quad (3.4)$$

where λ_i is a free parameter which determines the boundary condition.

The special case of $\lambda_i = 0$ corresponds to the Neumann boundary conditions. Another possible vertex condition is the Dirichlet condition. It is introduced when in the equation (3.2) $\lambda_i = \infty$.

In the case of Dirichlet boundary conditions the eigenfunctions vanish on all of the edges, except the edge e , where

$$\Psi_e(x) = \frac{e^{iA_e x}}{\sqrt{L_e}} \sin\left(\frac{n_e \pi x}{L_e}\right), \quad k_n^{(e)} = \frac{n_e \pi}{L_e}, \quad \text{for all } n_e > 0. \quad (3.5)$$

The resulting spectrum displays some Poissonian features when the lengths L_e are rationally independent.

The wave functions on the edges with the Neumann boundary conditions have the form [30]

$$\Psi_{i,j}(x) = \frac{C_{i,j} e^{iA_{i,j} x}}{\sin(kL_{i,j})} (\varphi_i \sin[(L_{i,j} - x)k]) + \varphi_j e^{-iA_{i,j} L_{i,j}} \sin(kx), \quad i < j. \quad (3.6)$$

3.2. Microwave networks

Microwave networks were introduced in Ref. [18]. They are structurally similar to quantum graphs and consist of coaxial cables (equivalent to bonds in quantum graphs) connected to joints (equivalent to nodes in quantum graphs); these elements are shown in Fig. 3.2.

A coaxial cable consists of the internal conductive wire of a radius r_1 and the conductive outer ring of an internal radius r_2 . The space between the conductors is filled with a homogeneous dielectric. The structure of a coaxial cable is shown in Fig. 3.3. If the frequency of the wave propagating inside the cable does not exceed the threshold value [32], only the fundamental transverse electromagnetic mode (so-called the Lecher

mode) can propagate inside it. The cutoff frequency, up to which only Lecher mode can propagate inside the cable, can be calculated as follows

$$v_c \approx \frac{c\sqrt{\epsilon}}{\pi(r_1 + r_2)}, \quad (3.7)$$

where c is the speed of light in vacuum, and ϵ the dielectric constant of the material that separates the conductors.

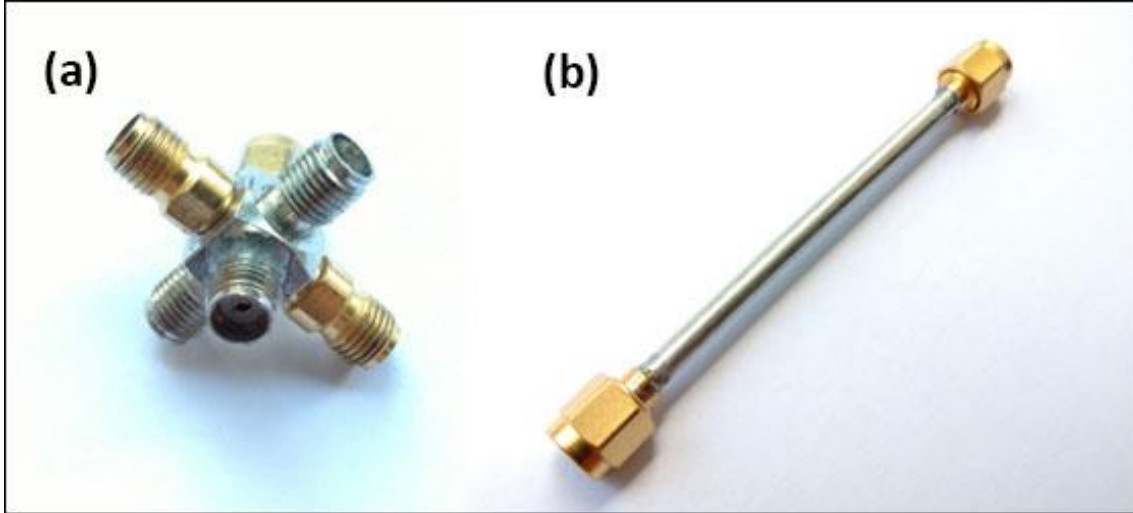


Fig. 3.2: (a) A six-arm joint with five male connectors that is used in the construction of microwave networks. (b) A coaxial cable with two female connectors.

Quantum graphs can be considered as the idealizations of physical networks in the limit where the widths of the wires are much smaller than their lengths.

The continuity equation for the charge $e_{ij}(x, t)$ and the current $J_{ij}(x, t)$ per unit length on the surface of the inner conductor of a cable [18] is given by

$$\frac{de_{ij}(x, t)}{dt} = -\frac{dJ_{ij}(x, t)}{dx}. \quad (3.8)$$

The potential difference is defined as follows

$$U_{ij}(x, t) = V_2^{ij}(x, t) - V_1^{ij}(x, t) = \frac{e_{ij}(x, t)}{C}, \quad (3.9)$$

where C is the capacitance of a cable per unit length, $V_1^{ij}(x, t)$ is the potential of the inner conductor of a coaxial cable, $V_2^{ij}(x, t)$ is the potential of the outer conductor of a coaxial cable.

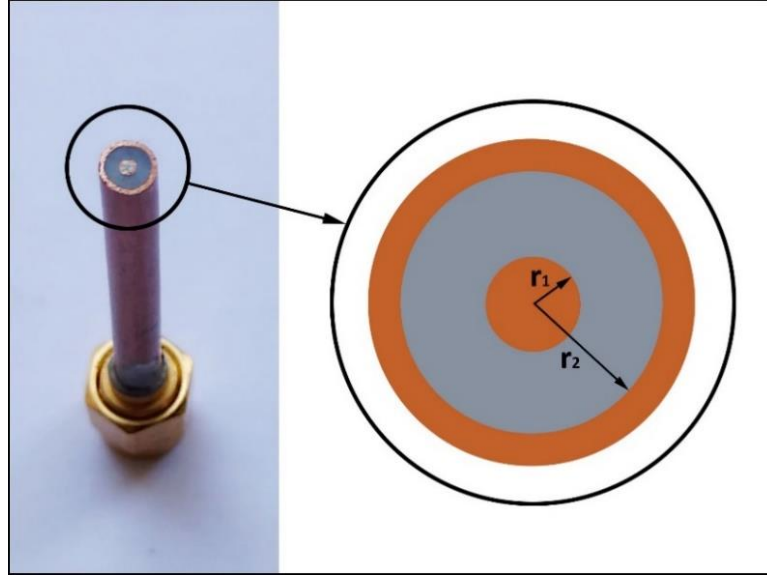


Fig. 3.3: The inner structure of a coaxial cable. Two conductors are separated by Teflon.

Assuming that the wave propagating along the cable is monochromatic $e_{ij}(x, t) = e^{-i\omega t} e_{ij}(x)$, $U_{ij}(x, t) = e^{-i\omega t} U_{ij}(x)$ and taking the spatial derivative of Eq. (3.9) one can obtain

$$\frac{d}{dx} U_{ij}(x) = - \left(R - \frac{i\omega L}{c^2} \right) J_{ij}(x, t), \quad (3.10)$$

where R is the resistance per unit length, L is the inductance per unit length, ω is the angular frequency and c is the speed of light in vacuum.

For $R = 0$ the Telegraph equation describing microwave networks has the following form

$$\frac{d^2}{dx^2} U_{ij}(x) + \frac{\omega^2 \epsilon}{c^2} U_{ij}(x) = 0, \quad (3.11)$$

where $\epsilon = LC$ is the dielectric constant, ω is the angular frequency, and $U_{ij}(x)$ is the potential difference between internal and external conductor of the coaxial cable.

It is easy to notice that if $\Psi_{i,j}(x) \Leftrightarrow U_{ij}(x)$, $k^2 \Leftrightarrow \frac{\omega^2 \epsilon}{c^2}$, the equations (3.2) and (3.11) are formally equivalent.

Due to equivalency of the one-dimensional Schrödinger equation that describes quantum systems and the Telegraph equation which describes microwave networks, such networks can be used to simulate quantum graphs. It was shown in Ref. [33] that graphs with 5-6 vertices exhibit best agreement with the RMT predictions. It was

demonstrated that increasing the number of vertices leads to the appearance of the localization phenomena that cause lower chaoticity of the system.

The microwave networks simulating quantum graphs with time violation symmetry can be constructed using non-reciprocal three-port passive devices called circulators [34]. A wave entering the circulator through the port 1, 2 or 3 exits at the port 2, 3, or 1, respectively, thus breaking time symmetry, not allowing the signal to return the same way (Fig. 3.4).

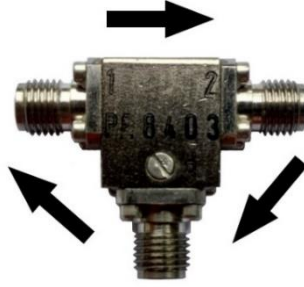


Fig. 3.4: A non-reciprocal three-port passive circulator PE8403. Arrows show signal propagation directions.

3.3. Quantum billiards

A billiard is a dynamical system of straight particle motion with specular reflection on boundaries. Such dynamic system is characterized by preserved energy, that means particle reflects from boundaries without loss of speed. A quantum billiard is a two-dimensional system in which a free particle moves in an infinite potential well in domain Ω . Motion of such a particle is described by the Schrödinger equation

$$-\frac{\hbar^2}{2m}\nabla^2\psi_n(q) = E_n\psi_n(q), \quad (\hbar = 2m = 1). \quad (3.12)$$

The Dirichlet boundary conditions implies that the potential is infinite outside the region Ω , but inside Ω is zero

$$\psi_n(q) = 0 \text{ for } q \notin \Omega. \quad (3.13)$$

The Neumann boundary conditions, with a unitary vector \vec{n} perpendicular to the border, is written as follows

$$\frac{d\psi_n(q)}{d\vec{n}} = 0 \text{ for } q \notin \Omega. \quad (3.14)$$

Generally, billiards are appropriate systems for studying the problems within the field of quantum chaos, because the degree of chaoticity of their classical dynamics only depends on their shape [9, 20, 35]. With the help of billiards the systems with integrable, chaotic or mixed motion can be studied.

The analytical results for the time-reversal invariant chaotic systems, the spectral properties of which are expected to coincide with those of the eigenvalues of random matrices from the Gaussian orthogonal ensemble, were verified using a microwave cavity with the shape of a Sinai billiard [36]. Rectangular billiards suits the best for the studies of integrable motion or that one which exhibits transition from integrable to chaotic motion (Fig. 3.5, panel (a)). A Sinai billiard is a rectangular-shaped billiard with sides a and b , with a circular scattering insert with a radius of r in the middle. Another popular billiard is a Bunimovich “stadium” billiard. A stadium is a domain bounded by two semicircles and two parallel straight segments (Fig. 3.5. panel (b)). Later, Bunimovich and Donnay extended this result to a wider class of domains in which semicircles can be replaced by general strictly convex curves and the straight segments are allowed to be nonparallel. A Bunimovich stadium and similar billiards are popular models in the theory of quantum chaos because of their simplicity and amenability to numerical methods [37].

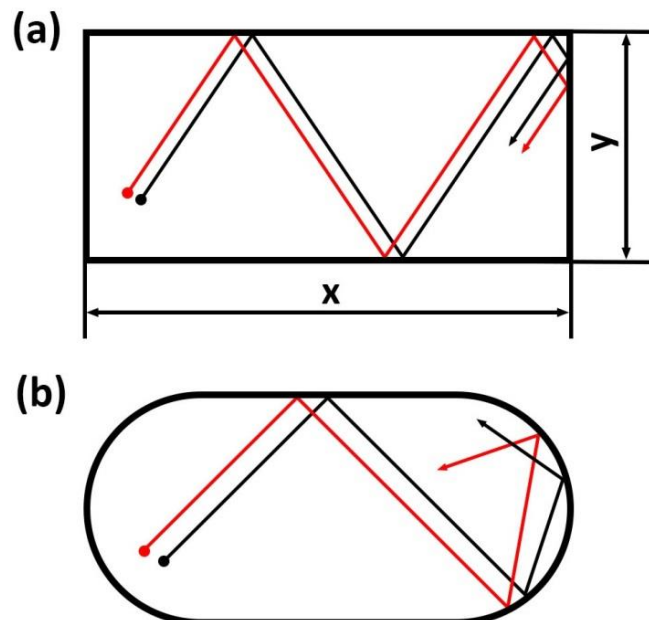


Fig. 3.5: (a) A regular billiard with regular motion (b) A stadium billiard with chaotic motion. The arrows illustrate evolution of particles depending on their initial positions.

3.4. Microwave cavities

Quantum billiards can be simulated by flat microwave cavities [38-43]. The analogy between microwave flat cavities and quantum billiards is based upon the equivalency of the Helmholtz equation, describing microwave cavities, and the two-dimensional Schrödinger equation, describing quantum systems.

The Helmholtz equations for magnetic and electric fields have the following forms

$$(\Delta + k^2)E = 0, \quad (3.15)$$

$$(\Delta + k^2)B = 0, \quad (3.16)$$

where $k = \frac{2\pi\nu\sqrt{\epsilon}}{c}$ is a wave vector, ν is frequency, ϵ is dielectric constant, and c is the speed of light.

In general, different boundary conditions apply to quantum-mechanical and electromagnetic systems, respectively. In the quantum-mechanical case, the wave function must be zero at the boundary, while in the electromagnetic case the tangential component of the electric field E and the normal component of the magnetic induction B must vanish at the boundary

$$n \times E = 0, \quad nB = 0, \quad (3.17)$$

n is a unitary vector perpendicular to the border of the cavity.

For cylindrical cavities, the transverse magnetic mode has a form

$$(x, y, z) = E(x, y) \cos\left(\frac{n\pi z}{d}\right), \quad n = 0, 1, 2, \dots \quad (3.18)$$

$$B_z(x, y, z) = 0, \quad (3.19)$$

where d is the height of the cavity and $E(x, y)$ satisfies the two-dimensional Helmholtz equation

$$\left(\Delta + k^2 - \left(\frac{n\pi}{d}\right)^2\right)E(x, y) = 0, \quad (3.20)$$

with Dirichlet boundary conditions on the side surface of the resonator S

$$E(x, y)|_S = 0. \quad (3.21)$$

Similarly, for a transverse electric mode

$$E_z(x, y, z) = 0, \quad (3.22)$$

$$B_z(x, y, z) = B(x, y) \sin\left(\frac{n\pi z}{d}\right), \quad n = 0, 1, 2, \dots \quad (3.23)$$

where $B(x, y)$ satisfies the two-dimensional Helmholtz equation

$$\left(\Delta + k^2 - \left(\frac{n\pi}{d}\right)^2\right) B(x, y) = 0, \quad (3.24)$$

with Neumann boundary conditions on the side surface of the resonator S

$$\nabla \perp B(x, y)|_S = 0. \quad (3.25)$$

If in two-dimensional cavities the excitation frequency ν is below $\nu_{max} = c/2d$, where c is the speed of light in the vacuum and d is the height of the cavity, only the transverse magnetic TM0 mode can be excited inside the cavity. $E_z(x, y)$ field in the cavity in this case is described by the following Helmholtz equation and the boundary condition.

$$(\Delta + k^2)E_z(x, y) = 0, \quad (3.26)$$

$$E_z(x, y)|_S = 0. \quad (3.27)$$

Thus, in the two-dimensional case quantum-mechanical and electromagnetic boundary conditions become identical. It is easy to notice that the Schrödinger equation (3.12) and the Helmholtz equation (3.26) formally are equivalent if $\Psi \Leftrightarrow E_z$, and $k^2 \Leftrightarrow \frac{2mE}{\hbar^2}$.

Obviously, walls in the cavities are not perfectly conductive as it is required by the boundary condition. If the conduction is finite the penetration depth is presented by formula

$$\delta = \sqrt{\frac{1}{\mu_0 \pi \nu \sigma}}, \quad (3.28)$$

where μ_0 is magnetic permeability of the vacuum, σ is conduction of the material from which cavity is made, and ν is frequency.

Energy losses in a cavity leads to resonance broadening, which in turn complicates the search for resonances in the experimental spectrum. The procedures of determination of resonances and the cases with incomplete spectra will be described in the following sections. Energy losses can be characterized with the help of the quality

parameter Q . The quality Q of a cavity is defined as $Q = \nu/\Delta\nu$, where ν is an eigenfrequency of a cavity and $\Delta\nu$ is its typical width. It can be approximated by

$$Q = \alpha \frac{V}{S\delta}, \quad (3.29)$$

where α is a geometric coefficient and V and S are the volume and the internal surface of a cavity, respectively.

CHAPTER 4

LONG-RANGE CORRELATIONS AND THE ELASTIC ENHANCEMENT FACTOR

4.1. Number variance and Dyson-Mehta statistic

The most common measures for the long-range spectral correlations are the number variance, and the spectral rigidity, also known as the Dyson-Mehta statistic. The variance $\Sigma^2(L)$ of the number of eigenvalues in an interval L is the expectation of the squared deviation of a random variable from its mean. Using this measure, it is possible to track how far the set of eigenvalues is spread out from its mean. The spectral rigidity $\Delta_3(L)$ is given by the least-squares deviation of the integrated resonance density of the eigenvalues from the straight-line best fitting it in the interval L [10].

The mean number of levels in the length interval L is given by probability $\varepsilon(k, L)$, $k = 0, 1, 2, \dots$ that a randomly chosen energy interval of length L contains exactly k levels

$$\langle n(L) \rangle = \sum_{k=1}^{\infty} k \varepsilon(k, L). \quad (4.1)$$

Then the number variance is defined as follows [44]

$$\Sigma^2(L, E) = \langle (n(L, E) - L)^2 \rangle = \sum_{k=0}^{\infty} (k - L)^2 \varepsilon(k, L). \quad (4.2)$$

Since the energy spectrum is unfolded

$$\langle n(L, E) \rangle = L. \quad (4.3)$$

In random matrix theory the number variance does not depend on energy. It is connected with the fact that the Gaussian ensembles are stationary over the energy spectrum.

For standard models one finds

$$\Sigma_{Poisson}^2(L) = L, \quad (4.4)$$

$$\begin{aligned} \Sigma_{GOE}^2(L) = \frac{2}{\pi^2} & \left(\log(2\pi L) + \gamma + 1 + \frac{1}{2} Si^2(\pi L) - \frac{\pi}{2} Si(\pi L) - \cos(2\pi L) \right. \\ & \left. - Ci(2\pi L) - Ci(2\pi L) + \pi^2 L \left(1 - \frac{2}{\pi} Si(2\pi L) \right) \right), \end{aligned} \quad (4.5)$$

$$\begin{aligned} \Sigma_{GUE}^2(L) = \frac{1}{\pi^2} & \left(\log(2\pi L) + \gamma + 1 - \cos(2\pi L) + Ci(2\pi L) \right. \\ & \left. + \pi^2 L \left(1 - \frac{2}{\pi} Si(2\pi L) \right) \right), \end{aligned} \quad (4.6)$$

where γ is Euler's constant, Ci and Si are the cosine and sine integral functions.

For large value of L equations (4.5) and (4.6) can be simplified to the following forms

$$\Sigma_{GOE}^2(L) = \frac{2}{\pi^2} \left(\log(2\pi L) + \gamma + 1 - \frac{\pi^2}{8} \right) + O(L^{-1}), \quad (4.7)$$

$$\Sigma_{GUE}^2(L) = \frac{1}{\pi^2} (\log(2\pi L) + \gamma + 1) + O(L^{-1}). \quad (4.8)$$

The spectral rigidity which measures the two-point correlation, in turn, can be written as follows

$$\Delta_3(L, E) = \langle \min_{A,B} \frac{1}{L} \int_{-L/2}^{L/2} de (N(E+e) - A - Be)^2 \rangle. \quad (4.9)$$

The brackets denote a local average with an effective width ΔE .

For short correlation lengths, $L \ll 1$, the spectral rigidity is independent of the underlying spectrum

$$\Delta_3(L) \sim \frac{L}{15}. \quad (4.10)$$

Both functions, $\Sigma^2(L)$ and $\Delta_3(L)$, can be defined using the two-point cluster function [45]

$$\Sigma^2(L) = L - 2 \int_0^L (L-x) Y_2(x) dx, \quad (4.11)$$

$$\Delta_3(L) = \frac{L}{15} - \frac{1}{15L^4} \int_0^L (l-x)^3 (2L^2 - 9xL - 3x^2) Y_2(x) dx. \quad (4.12)$$

For the Gaussian Orthogonal and Unitary ensembles, the two-point cluster function can be expressed as

$$Y_2(x) = \left(\frac{\sin(\pi x)}{\pi x}\right)^2 - \left(\int_0^{\pi x} \frac{\sin(t)}{t} dt - \pi \in(x)\right) \cdot \left[\frac{\cos(\pi x)}{\pi x} - \frac{\sin(\pi x)}{(\pi x)^2}\right], \quad (4.13)$$

$$Y_2(x) = \left(\frac{\sin(\pi x)}{\pi x}\right)^2. \quad (4.14)$$

Here, $\in(x) = \pm 1/2$ if $x > 0$ or $x < 0$ and $\in(x) = 0$ if $x = 0$.

For uncorrelated levels, one has essentially by the definition $Y_2(x) \equiv 0$ [46].

4.2. $1/f^\alpha$ noise

Many physical fluctuations have empirical spectral densities that are nearly proportional to $1/f^\alpha$ noises [47]. In engineering, electronics, physics, and many other fields, the color of noise refers to the power spectrum of a signal produced by a stochastic process. This kind of noises has been detected in condensed matter systems, traffic engineering, DNA sequence, quasar emissions, river discharge, human behavior, heartbeat and dynamic images, among many others. Despite this ubiquity, there is no universal explanation about this phenomenon. It does not arise as a consequence of particular physical interactions, but it is a generic manifestation of complex systems [48]. Looking ahead, the energy spectra of regular and chaotic quantum systems are characterized by $1/f^\alpha$, red and pink noises, respectively [49]. Red noise or Brownian (Brown) noise, is the kind of signal produced by Brownian motion, its spectral density is inversely proportional to f^2 . Pink noise is a signal with the power spectral density inversely proportional to the frequency of the signal.

Let's treat an energy spectrum as a discrete signal, and the sequence of energy levels as a time series. Further, after performing unfolding procedure, let's calculate the deviation of the $(n + 1)$ th level from its mean value

$$\delta_n = \sum_{i=1}^n (s_i - \langle s \rangle) = \sum_{i=1}^n w_i, \quad (4.15)$$

where index n runs from 1 to $N - 1$ (N is the dimension of the spectrum), w_i is the fluctuation of the i th spacing from its mean value.

Now it is possible to define another statistical measure which can be used to characterize long-range spectral fluctuations – the power spectrum $S(k)$ of discrete and finite series δ_n

$$S(k) = |\hat{\delta}_k|^2, \quad (4.16)$$

where $\hat{\delta}_k$ is the Fourier transform of δ_n deviations

$$\hat{\delta}_k = \frac{1}{\sqrt{N}} \sum_n \delta_n \exp\left(\frac{-2\pi i k n}{N}\right). \quad (4.17)$$

It turned out that the average power spectrum $\langle S(k) \rangle$ follows closely a power law

$$\langle S(k) \rangle \sim \frac{1}{k^\alpha}, \quad (4.18)$$

where $\alpha = 2$ corresponds to the Poisson spectrum while the energy spectra of chaotic quantum system are characterized by $\alpha = 1$.

In Ref. [50] the analytical expression for $\langle S(k) \rangle$ was derived on the basis of RMT

$$\langle S(k) \rangle = \frac{1}{4\pi^2} \left(\frac{K\left(\frac{k}{N}\right) - 1}{\left(\frac{k}{N}\right)^2} + \frac{K\left(1 - \frac{k}{N}\right) - 1}{\left(1 - \frac{k}{N}\right)^2} \right) + \frac{1}{4\sin^2\left(\frac{\pi k}{N}\right)} + \Delta. \quad (4.19)$$

Here, $\Delta = 1/12$ for chaotic systems and $\Delta = 0$ for integrable systems and $K(\tau)$ is the spectral form factor. Defining $\tau = k/N$

$$K^{Poisson}(\tau) = 1, \quad (4.20)$$

$$K^{GOE}(\tau) = \begin{cases} 2\tau - \tau \log * (1 + 2\tau), & \tau \leq 1 \\ 2 - \tau \log \left(\frac{2\tau + 1}{2\tau - 1} \right), & \tau \geq 1 \end{cases} \quad (4.21)$$

$$K^{GUE}(\tau) = \begin{cases} \tau, & \tau \leq 1 \\ 1, & \tau \geq 1 \end{cases} \quad (4.22)$$

For $\tau \ll 1$ the average power spectrum approaches a familiar power-law behavior $\langle S(k) \rangle \sim \frac{1}{(k/N)^\alpha}$, which can be summarized for chaotic systems as follows

$$\langle S(k) \rangle_\beta = \frac{N}{2\beta\pi^2 k}, \quad (4.23)$$

where β stands for the repulsion parameter characterizing the ensembles, $\beta = 1$ for GOE and $\beta = 2$ for GUE.

For integrable systems the equation (4.19) reduces to the following form

$$\langle S(k) \rangle = \frac{N^2}{4\pi^2 k^2}. \quad (4.24)$$

The above expressions emphasize that the energy fluctuations exhibit $1/f$ pink noise in chaotic systems and $1/f^2$ red noise in the integrable ones. In the order-to-chaos transition, the chaoticity of a quantum system is usually qualitatively assessed by using short- and long-range correlators such as the nearest-neighbor spacing distribution or the level variance. In the power spectrum approach, the exponent changes smoothly from $\alpha = 2$ for a regular system to $\alpha = 1$ for a chaotic system. Parameter α provides an intrinsic quantitative measure of the dynamical features of the investigated system [48].

4.3. The elastic enhancement factor

The elastic enhancement factor $W_{S,\beta}$, where $\beta = 1$ or 2 is the symmetry index for systems with preserved and broken time-reversal symmetry, respectively, was introduced in 1961 by P. A. Moldauer [51]. It can be defined as the ratio of variances of diagonal elements of the two-port scattering matrix \hat{S} to the off-diagonal element of this matrix [52-54]

$$W_{S,\beta} = \frac{\sqrt{\text{var}(S_{aa})\text{var}(S_{bb})}}{\text{var}(S_{ab})}, \quad (4.25)$$

where $\text{var}(S_{ab})$ is the variance of the matrix element S_{ab}

$$\text{var}(S_{ab}) \equiv \langle |S_{ab}|^2 \rangle - |\langle S_{ab} \rangle|^2, \quad (4.26)$$

of the two-port scattering matrix \hat{S} , which relates the outgoing scattered wave amplitudes to the incoming waves

$$\hat{S} = \begin{bmatrix} S_{aa} & S_{ab} \\ S_{ba} & S_{bb} \end{bmatrix}. \quad (4.27)$$

The elastic enhancement factor is often considered in nuclear physics [52, 55, 56] as well as in the other fields [53, 54]. Fiachetti and Michelson were the first who conjectured that in electromagnetic fields in the reverberating chambers, where a mode stirrer is put in a sequence of fixed positions, the ratio of variances of the scattering elements exhibits the universal behavior $W_{S,\beta=1} = 2$ [57]. The elastic enhancement factor was tested with microwave cavities [57-60] and networks [19, 61, 62] simulating quantum billiards and quantum graphs, respectively. The elastic enhancement factor can be used to study realistic open systems in the presence of strong absorption which makes it especially valuable in the experimental research.

The elastic enhancement factor $W_{S,\beta}$ can be parametrized by the absorption strength

$$\gamma = \frac{2\pi\Gamma}{\Delta}, \quad (4.28)$$

where Γ is the average resonance width and Δ is the mean level spacing [53, 54]. Microscopically, the absorption strength can be modeled by means of a huge number of open, coupled to continuum channels “c”

$$\gamma = \sum_c T_c = 1 - \langle |S_{cc}|^2 \rangle, \quad (4.29)$$

where $\langle S_{cc} \rangle$ stands for the average S matrix [54] and T_c is known as transmission coefficients.

The cases where $T_c \ll 1$ and $T_c = 1$ correspond to almost closed or perfectly open channel “c”, respectively. In Ref. [52] Kharkov and Sokolov showed that the elastic enhancement factor of open systems depends on the openness parameter η , which is basically described by the same formula as the absorption strength γ .

The elastic enhancement factor can be written in terms of the absorption γ and symmetry class β of the system in the following way [53]

$$W_{S,\beta} = 2 + \delta_{1\beta} - \int_0^\infty ds e^{-s} b_{2,\beta} \left(\frac{s}{\gamma} \right), \quad (4.30)$$

$$b_{2,\beta=1}(\tau) = [1 - 2\tau + \tau \log(1 + 2\tau)]\theta(1 - \tau) + \left[\tau \log \frac{2\tau + 1}{2\tau - 1} - 1 \right] \theta(\tau - 1), \quad (4.31)$$

$$b_{2,\beta=2}(\tau) = (1 - \tau)\theta(1 - \tau), \quad (4.32)$$

where $b_{2,\beta} \left(\frac{s}{\gamma} \right)$ is the spectral form factor, $\theta(\cdot)$ is the Heaviside step function and τ is time expressed in Heisenberg time units.

One can define $W_{S,\beta}$ in the limiting cases of weak or strong absorption by making use of $b_{2,\beta}(\infty) = 0$ and $b_{2,\beta}(0) = 1$

$$W_{S,\beta} = \begin{cases} 2 + \delta_{1\beta} & \text{at } \gamma \ll 1 \\ 1 + \delta_{1\beta} & \text{at } \gamma \gg 1 \end{cases} \quad (4.33)$$

The elastic enhancement factor might depend both on the parameter γ and on the coupling to the system in the cases of weak or intermediate absorption [58]. With

increasing of absorption, the elastic enhancement factor decays monotonically reaching the value 2 for a system with preserved time reversal symmetry, and the value 1 for a system with broken time reversal symmetry. Turning to the work of Fiachetti [63], in the case of a stochastic environment, the elastic enhancement factor should have the universal value $W_{S,\beta} = 2$. Such a stochastic environment can be characterized by a statistically isotropic scattering matrix. According to Sokolov and Zhirov [64] in the case of the two-channel problem with internal absorption and time-reversal symmetry, the elastic enhancement factor can take values between 3 and 2, depending on the transmission coefficient T and internal absorption.

CHAPTER 5

MISING LEVELS IN SPECTRAL FLUCTUATION

The completeness of energy spectra is rather a rare situation. In the experimental investigations loss of levels is connected with both small amplitudes of some resonances and with a large density of states. Even in the case of microwave networks which are characterized by relatively small losses the complete energy spectra are hard to observe. Therefore, such a value possesses the procedure which allows to deal with incomplete spectra. The analytical expressions for the incomplete spectra, i.e. such which contain missing-level, were derived by Bohigas and Pato in Ref. [45]. The presented RMT calculations are parametrized by the fraction of observed levels φ , which can take the values between 0 and 1.

The nearest-neighbor spacing distribution $p(s)$ is expressed in terms of the $(n + 1)$ st nearest-neighbor spacing distribution $P\left(n, \frac{s}{\varphi}\right)$,

$$p(s) = \sum_{n=0}^{\infty} (1 - \varphi)^n P\left(n, \frac{s}{\varphi}\right). \quad (5.1)$$

$P(n, s)$ can be expressed in the form [65]

$$P(n, s) = \zeta s^{\mu} e^{\xi s^2}. \quad (5.2)$$

The repulsion exponent μ equals 1 for the nearest, 4 for the second-nearest, and 8 for the third-nearest neighbors in the GOE case. For GUE systems the corresponding numbers are 2, 7 and 14, respectively. The coefficients ζ and ξ are obtained from normalization procedure

$$\int P(n, s) ds = 1, \quad (5.3)$$

$$\int s P(n, s) ds = n + 1. \quad (5.4)$$

For a system which possesses the GOE symmetry, the first and second terms in Eq. (5.1) is also approximated by

$$P\left(0, \frac{s}{\varphi}\right) = \frac{\pi s}{2\varphi} \exp\left[-\frac{\pi}{4}\left(\frac{s}{\varphi}\right)^2\right], \quad (5.5)$$

$$P\left(1, \frac{s}{\varphi}\right) = \frac{8}{3\pi^3} \left(\frac{4}{3}\right)^5 \left(\frac{s}{\varphi}\right)^4 \exp\left[-\frac{16}{9\pi}\left(\frac{s}{\varphi}\right)^2\right]. \quad (5.6)$$

When $\varphi = 1$, the above formulas are reduced to a Wigner surmise formula for the NNSD in a case of $P(0, s)$ and to the NNSD of the symplectic ensemble with $\langle s \rangle = 2$ in the case of $P(1, s)$. For higher $n = 2, 3, \dots$ the spacing distributions $P\left(n, \frac{s}{\varphi}\right)$ are well approximated by their Gaussian asymptotic forms, centered at $n + 1$

$$P\left(n, \frac{s}{\varphi}\right) = \frac{1}{\sqrt{2\pi V^2(n)}} \exp\left[-\frac{\left(\frac{s}{\varphi} - n - 1\right)^2}{2V^2(n)}\right], \quad (5.7)$$

with the variances

$$V^2(n) \simeq \Sigma^2(L = n) - \frac{1}{6}. \quad (5.8)$$

The spectral rigidity of the spectrum $\Delta_3(L)$ in the presence of missing levels $\delta_3(L)$ [45] may be expressed in terms of those for the complete spectra $\Delta_3(L)$

$$\delta_3(L) = (1 - \varphi) \frac{L}{15} + \varphi^2 \Delta_3\left(\frac{L}{\varphi}\right). \quad (5.9)$$

The number variance $\sigma(L)$ formula takes the following form when missing states are considered

$$\sigma(L) = (1 - \varphi)L + \varphi^2 \Sigma^2\left(\frac{L}{\varphi}\right). \quad (5.10)$$

The analytical expression for the power spectrum of level fluctuations is given in Ref. [66]

$$\left\langle s\left(\frac{k}{N}\right) \right\rangle = \frac{\varphi}{4\pi^2} \left[\frac{K\left(\varphi \frac{k}{N}\right) - 1}{\left(\frac{k}{N}\right)^2} + \frac{K\left(\varphi \left(1 - \frac{k}{N}\right)\right) - 1}{\left(1 - \frac{k}{N}\right)^2} \right] + \frac{1}{4\sin^2\left(\pi \frac{k}{N}\right)} - \frac{\varphi^2}{12}. \quad (5.11)$$

Here, $0 \leq \frac{k}{N} = \tau \leq 1$ and $K(\tau)$ is the spectral form factor, which equals to the Eq. (4.21) for the GOE systems and to the Eq. (4.22) for the GUE systems. When $\varphi = 1$ this formula is reduced to the formula studied in Refs. [49, 50].

In the case of incomplete spectra the long-range correlations: the number variance, the spectral rigidity and the power spectrum of level fluctuations are especially interesting because they can be used to find the number of missing levels. In the search of missing levels it is particularly important that the aforementioned measures are very sensitive to a number of missing levels. Such properties are of great value in the experimental investigations.

CHAPTER 6

THE ELASTIC ENHANCEMENT FACTOR AS A MEASURE OF INTERNAL CHAOS

In this section I will present the results of an experimental study of the elastic enhancement factor for a microwave rough and rectangular cavities simulating a two-dimensional chaotic and partially chaotic quantum billiards, respectively. It will be shown that a transient region between regular and chaotic dynamics in microwave rectangular cavity is characterized by the parameter of chaoticity $k = 2.8$. The elastic enhancement factor for the microwave rough cavity appeared to be smaller than those obtained within the framework of random matrix theory and on average above the theoretical results of V. Sokolov and O. Zhirov [64] predicted for chaotic systems. Both cavities are characterized by the presence of comparable moderate absorption.

The two-port scattering matrix \hat{S} required for the calculation of the elastic enhancement factor was measured using a vector network analyzer Agilent E8364B shown in Fig. 6.1. The operating frequency range of the analyzer is 10 MHz – 50 GHz. Coupling to the experimental setups was performed with the help of the flexible microwave cables HP 85133-616 and HP 85133-617. In the case of the two-port measurement the scattering matrix \hat{S} is described by the expression (4.27). The scattering matrix elements S_{aa} and S_{bb} are connected with the signals reflected to the ports a and b of the analyzer, while the elements S_{ab} and S_{ba} are connected with the signals transmitted between the ports. For a single port measurement, a single-channel coupling of the experimental setup is foreseen; in this case the matrix S can be expressed with the help of a reflection coefficient R

$$S = \sqrt{R}e^{i\theta}, \quad (6.1)$$

where θ is a phase.

Looking ahead, the transient region between regular and chaotic dynamics, was investigated by using a microwave rectangular cavity that simulates a two-dimensional

(2D) quantum billiard. The structure of such a cavity is simple: the brass bars of 8 mm high form the rectangular shape which was closed with the brass plates from both sides, forming the bottom and the upper walls of the cavity. Figure 6.2 shows the scheme of the rectangular microwave cavity, which was used in measurements of the two-port scattering matrix \hat{S} . In order to conduct these measurements, the two antennas wires of diameter 0.9 mm were protruded 3 mm inside the cavity. The positions of the antennas play significant role in the measurements. Therefore, the measurements were made for 10 different positions of the antennas. This was achieved using five holes A_1, A_2, A_3, A_4 and A_5 in the upper plate of the cavity. While the microwave antennas were introduced into the two chosen holes, the rest of the holes were closed with the brass plugs. The width of the rectangular cavity was equal to $L_2 = 20$ cm. The different realizations of the cavity were created by changing the position of one of the walls (see Fig. 6.2). The length of the cavity was changed from $L_1 = 41.5$ to 36.5 cm in 25 steps of 0.2 cm length.



Fig. 6.1: A photo of the vector network analyzer Agilent E8364B.

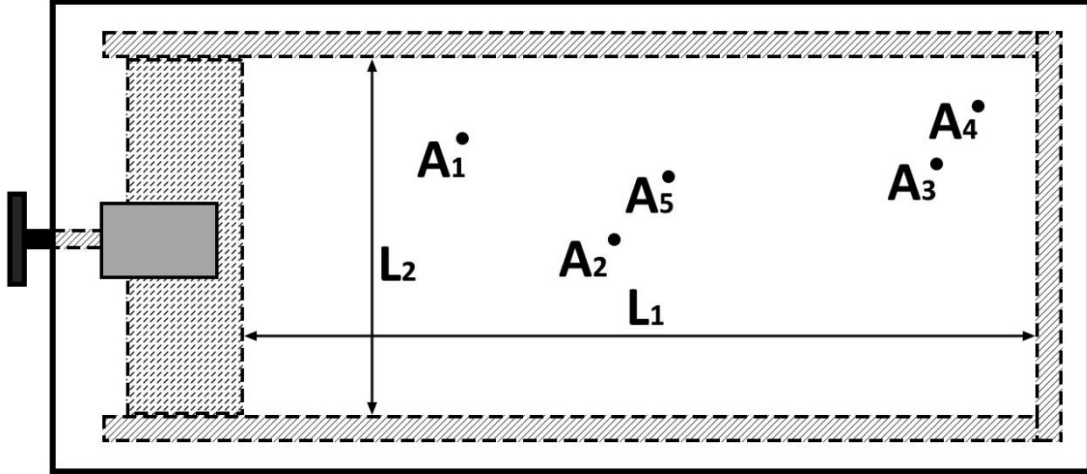


Fig. 6.2: A scheme of the rectangular cavity. With the respect to the higher right corner the holes A_1 , A_2 , A_3 , A_4 and A_5 are located at (31.6, 5.2) cm, (21.5, 14.1) cm, (5.7, 8.2) cm, (3.6, 2.9) cm and (20.6, 7.7) cm, respectively.

The rough microwave cavity made of aluminum was also measured for the comparison (see Figure 6.3). Such a cavity exhibits fully chaotic behavior and simulates a quantum chaotic billiard. The rough cavity is composed of the two sidewall segments of height 8 mm. It is closed from the top and the bottom by two plates. The rough surface (marked (1) in Fig. 6.3) is described by the function $r(\theta) = r_0 + \sum_{i=2}^M a_i \sin(i\theta + \phi_i)$, where the mean radius $r_0 = 20.0$ cm, $M = 20$, and $0 \leq \theta < \pi$. The amplitudes a_i and the phases ϕ_i are uniformly distributed on $[0.084, 0.091]$ cm and $[0, 2\pi]$, respectively. The straight side wall is marked with (2) in Fig. 6.3. To create different realizations of the cavity, the scatterer was moved inside the cavity along the sidewall (1). The metallic scatterer having the area $A_{\text{scatterer}} \approx 9$ cm² and the perimeter $P_{\text{scatterer}} \approx 26$ cm was moved using an external magnet.

The cutoff frequency in the case of microwave cavities is calculated from the formula

$$v_{\max} = \frac{c}{2d'} \quad (6.2)$$

where c is the speed of light and d is the height of the cavity.

Thereby, the height $d = 8$ mm for the both cavities provides the equivalence between the two-dimensional Schrödinger equation and the Helmholtz equation up to

$\nu_{max} = 18.7$ GHz. The measurements were done in a frequency range $\nu = 16 - 18.5$ GHz.

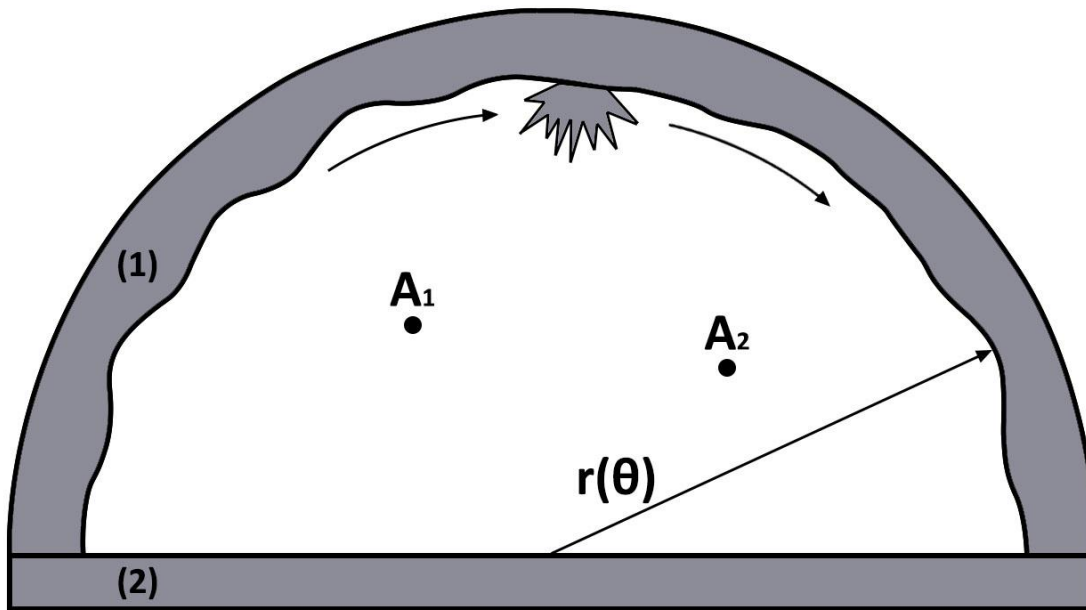


Fig.6.3: A scheme of the rough cavity. With the respect to the lower left corner the holes A_1 and A_2 are located at $(11.3, 10.6)$ cm and $(29.3, 8.4)$ cm, respectively.

In the first step of the analysis the properties of microwave cavities were investigated using the nearest-neighbor spacing distribution $P(s)$. The NNSD, calculated for the rectangular cavity, is illustrated in Figure 6.4(a) with red histograms. Results were averaged over 30 microwave rectangular cavity configurations in the frequency range 16 – 17 GHz. The obtained results clearly departure from the theoretical prediction of the Poisson distribution (full blue line). At the same time, they don't match the prediction of GOE in RMT (dashed black line). The analytical curves for the NNSD in the case of the orthogonal ensemble were approximated by Eq. (2.21) while the Poisson distribution has a simple form Eq. (2.24). Fig. 6.4(a) shows that in the case of the rectangular billiard for $0 < s < 2$ we deal with the transition from chaotic to integrable dynamics. This behavior differs from the one observed by Robnik and Veble in Ref. [67] in numerical calculations performed for the rectangular billiards, since the departure from the Poisson distribution is noticeable not only for very small s , but also for much larger s .

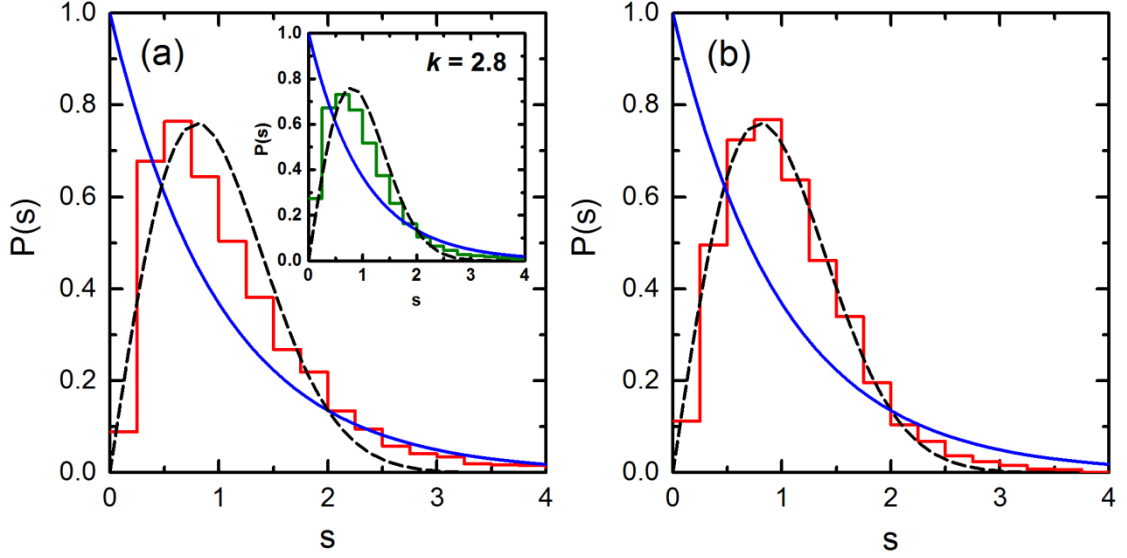


Fig. 6.4: (a) The nearest-neighbor spacing distribution $P(s)$ for the microwave rectangular cavity (red histogram). The insert shows the numerical reconstruction of the NNSD with the chaoticity parameter $k = 2.8$ (green histogram) (b) The nearest-neighbor spacing distribution $P(s)$ for the microwave rough cavity (red histogram). The results are compared with the theoretical predictions for the GOE (black dashed line) and the Poisson (blue solid line) distributions.

In order to numerically analyze our experimental results, I used the Porter-Rosenzweig RMT model [68]. According to this model, a random matrix a_{ij} can be defined as follows

$$a_{ij} = g_{ij}[\delta_{ij} + \lambda(1 - \delta_{ij})], \quad (6.3)$$

where g_{ij} is a symmetric matrix that belongs to GOE symmetry class, $\lambda = k/N$ is the transition parameter, N is the size of the matrix a_{ij} . The off-diagonal elements g_{ij} are independently Gaussian-distributed with the same variance $\text{var}(g_{ij}) = 1$ and the mean equals zero. The diagonal elements g_{ii} are independently distributed with the variance $\text{var}(g_{ii}) = 2$.

The numerical NNSDs were calculated on the basis of 100 random matrices of the size 200×200 possessing different chaoticity parameter k . Thereafter, the least square deviation from the experimental results was estimated for the each numerical NNSD, yielding the best fitted chaoticity parameter k . The inset in Fig. 6.4(a) shows the

numerically reconstructed nearest-neighbor spacing distribution (green histogram) with the chaoticity parameter $k = 2.8 \pm 0.5$.

In Fig. 6.4(b) the experimental NNSD for the rough cavity (red histogram) is presented. The result, as expected, matches the theoretical curve predicted by the GOE distribution (dashed black line), which corresponds to a completely chaotic system. Small discrepancies at high s can be connected with some unresolved resonances or the fingerprints of nonuniversal behaviors.

The next step of the analysis was a calculation of the elastic enhancement factor $W_{S,\beta=1}$ (see the Eq. (4.25)) of the two-port scattering matrix \hat{S} for the microwave rectangular and rough cavities. For the integrable systems with time-reversal symmetry, the elastic enhancement factor $W_{S,\beta=1} = 3$, while $2 \leq W_{S,\beta=1} \leq 3$ for the GOE systems and $1 \leq W_{S,\beta=2} \leq 2$ for the GUE ones. The elastic enhancement factor has already proven itself as a good measure capable to determine the chaoticity and symmetry classes in quantum graphs even in a presence of strong absorption. In this section there're presented numerical and experimental studies of the elastic enhancement factor for the microwave cavities in the presence of moderate absorption γ . Thereafter, for the systems with preserved TRS, the abbreviation $W \equiv W_{S,\beta=1}$ will be used.

The parameter γ was estimated by M. Ławniczak by adjusting the theoretical mean reflection coefficients, parametrized by the parameters γ_j ,

$$\langle R \rangle_{th}^{(j)} = \int_0^1 dR RP(R), \quad (6.4)$$

to the experimental ones $\langle R \rangle^{(j)}$, obtained after eliminating the direct processes [69-71]. In the considered frequency range, the absorption γ for the rectangular cavity had values which varied from 5.2 to 7.4, while for the rough cavity these values were from 5.3 to 6.8. In fact, the ohmic losses of the cavity's material wasn't the only factor that influenced the internal absorption of the cavity. In the reality, it is strongly modified by the precision of manufacturing and assembling of the cavity.

In the case of the rectangular cavity the elastic enhancement factor was obtained in the frequency range 16 – 18.5 GHz and was averaged over 250 different realizations of the cavity in the frequency window $\left(\nu - \frac{\delta\nu}{2}, \nu + \frac{\delta\nu}{2}\right)$ where $\delta\nu = 0.5$ GHz (red dots in Fig. 6.6(a)). These realizations were created by the length adjustment of one of the walls of the cavity and by changing the antennas positions. The RMT results (empty

green dots in Fig. 6.6(a)) were evaluated using the Eq. (4.30) and compared with those, that were obtained experimentally. The RMT limits for very strong ($W = 2$) and very low ($W = 3$) absorptions are illustrated in Fig. 6.6 with blue and vine dashed lines, respectively. The results, obtained experimentally, lie below the value $W = 3$, that strongly suggests that the system, simulated by the rectangular cavity, exhibits dynamics which departs from the integrable one. According to Petr Šeba [72], such a departure can be connected with the scattering on the antennas. This phenomenon was thoroughly analyzed by Tudorovskiy et al. in Ref. [73].

In the case of the rectangular and rough billiards the 3 mm long antennas were characterized by the average transmission coefficient $\bar{T} = \frac{1}{2}(T_a + T_b) \simeq 0.75$.

The averaged transmission coefficient in a two-port scattering matrix measurements was evaluated from the relation

$$\bar{T} = \frac{1}{2} \sum_{j=a,b} T_j, \quad (6.5)$$

where $T_j = 1 - |\langle S_{jj} \rangle|^2$, and the index $j = a, b$ denotes the port of the analyzer.

The transmission coefficients for the both rectangular and rough cavities are shown in Fig. (6.5) as a function of the frequency.

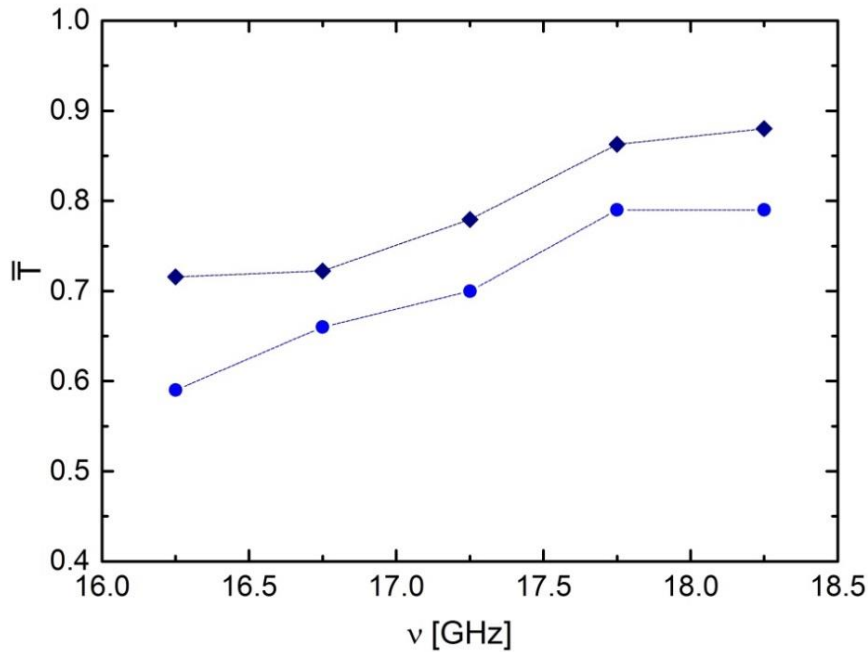


Fig. 6.5: The average transmission coefficients of the 3 mm long antennas. Dark blue diamonds mark the coefficient of the rough cavity. Blue circles stand for the coefficient of the rectangular cavity.

The elastic enhancement factor W of the two-port scattering matrix \hat{S} , calculated for the rough cavity, is shown in Fig. 6.6(b) with red diamonds. The different realizations of the cavity were measured in the frequency range 16 – 18.5 GHz and created by over 105 different scatterer positions. This frequency window, near the maximum threshold, was chosen intentionally to avoid the regimes of localization and Wigner ergodicity. These regimes, which should appear for lower frequencies, are reported in Refs. [43, 74, 75]. The rough cavity in the studied frequency range is in the regime of Shnirelman ergodicity, i.e., a fully chaotic one. The introduction of the perturber inside the cavity extends the Shnirelman ergodicity regime to the lower frequencies $\nu = 6 - 9$ GHz. The experimental values of the elastic enhancement factor are compared to the theoretical ones calculated in the framework of RMT (green empty diamonds).

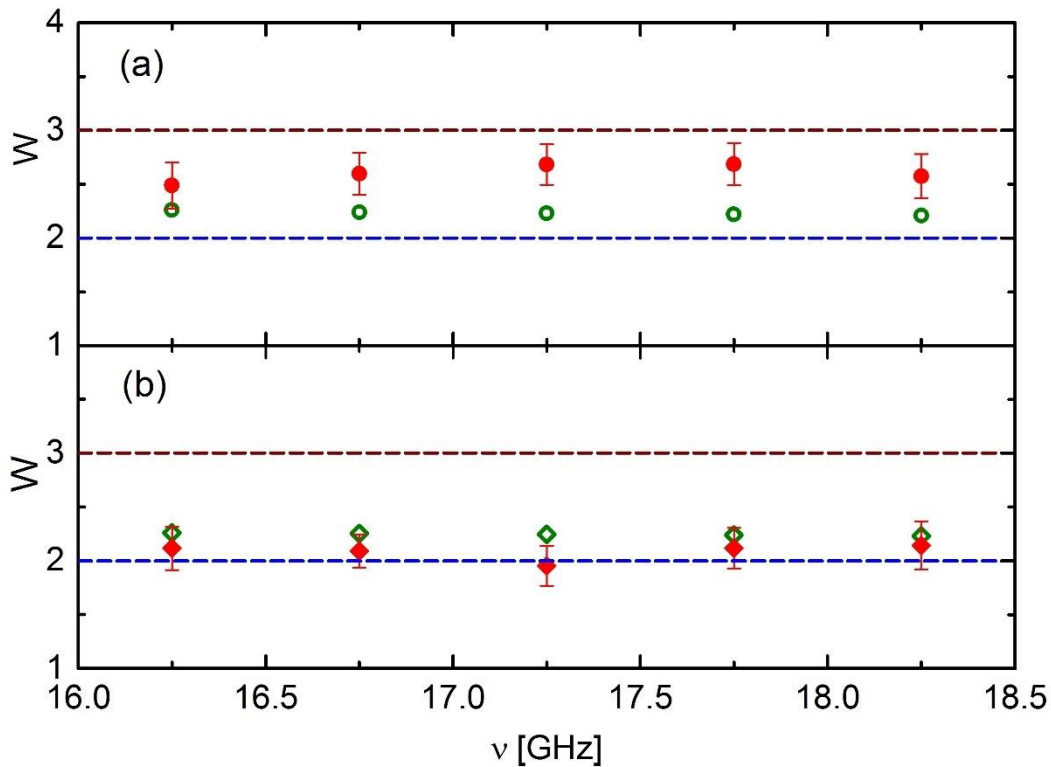


Fig. 6.6: (a) The elastic enhancement factor W of the two-port scattering matrix \hat{S} of the rectangular cavity (red dots) compared to the RMT predictions (green circles). (b) The elastic enhancement factor W of the two-port scattering matrix \hat{S} of the rough cavity (red diamonds) compared to the RMT predictions (empty green diamonds).

The elastic enhancement factor measured for the rectangular cavity lays significantly higher than the one obtained for the microwave rough cavity. Considering that both cavities are characterized by similar moderate absorption strength, the obtained results suggest that the elastic enhancement factor depends very sensitively on the level of chaoticity of the studied systems. The results obtained for the microwave rough cavity are smaller than those obtained within the framework of RMT. At the same time, on average, they are above the theoretical results predicted by Sokolov and Zhirov for the two-channel coupling [64]. The obtained results strongly suggest that the elastic enhancement factor can be successfully used as a measure of internal chaos even for systems with significant absorption or openness.

CHAPTER 7

MISSING LEVEL STATISTIC IN MICROWAVE NETWORKS

Missing levels are inevitable in the majority of real physical systems and experimental investigations due to number of reasons, such as the power absorption, quasi- or real level degeneration, etc. Therefore, it is important to have some procedures that could be used in the analysis of the systems that exhibit missing levels. I will demonstrate experimentally that the information on missing levels may be obtained on the basis of commonly used statistical measures for short- and long-range spectral fluctuations [45]. It's worth noting, that for long-range spectral fluctuations the effect of missing levels is much more significant than for the short-range correlators. One of such a remarkable long-range spectral fluctuations measure is the power spectrum [76].

7.1. Missing level statistics of microwave networks with broken TRS

The complete violation of time-reversal symmetry (TRS) in microwave billiards is difficult, if not impossible. Despite the fact that scattering systems with broken TRS were studied thoroughly in experiments with microwave billiards [60, 77], it is much more convenient to use microwave graphs for that reason. Microwave networks simulating quantum graphs with broken TRS can be relatively easily constructed using microwave circulators (Fig. 3.4). Such graphs were studied extensively in Refs. [4, 29, 61, 70, 78].

Fig. 7.1 shows a scheme of the six-vertex microwave network containing four phase shifters and five circulators. Such a network was used in the study of missing levels statistics. The details of the real experimental network are shown in Fig. 7.2. Five vertices of the graph consisted circulators which were coupled by junctions to four-arm microwave connectors (Fig. 7.2(a)). The six-arm microwave connector (Fig. 7.2(b)) was

used to connect the network to the VNA (Fig. 6.1) in order to measure the one-port scattering matrix S (Eq. (6.1)).

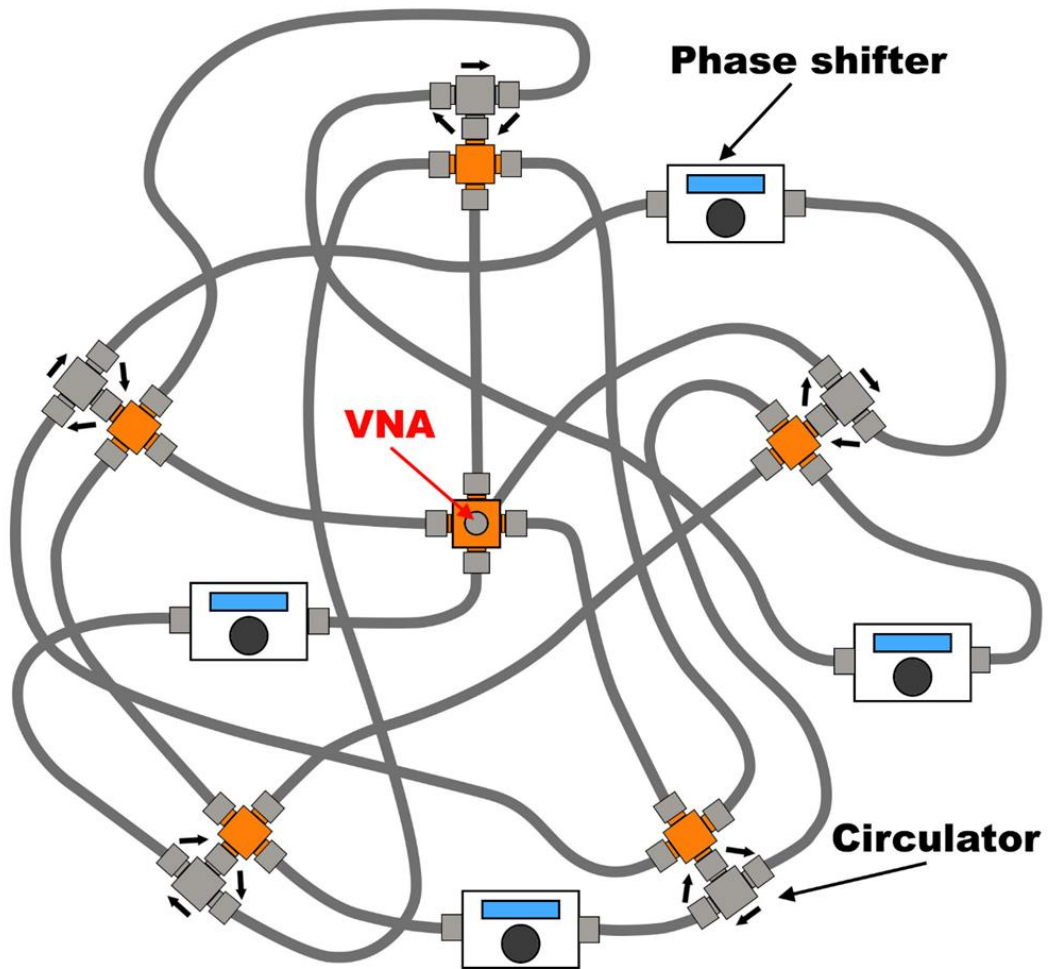


Fig. 7.1: A scheme of a six-vertex fully connected microwave network with broken TRS. Optical lengths of four bounds were changed using phase shifters. Directions of propagating signals are marked close to the circulators; the VNA was connected to vertex shown in the middle of a figure.

A microwave phase shifter (ATM PNR P1507D) is a two-port device capable of producing delay of a microwave signal propagating through it (Fig. 7.3). In this way, it was possible to control accurately the length of a graph, what is very important in the experiment. By increasing the length of one bond and decreasing the length of another one by the same value, the total length of the network remains constant. This allowed to create a large number of graph realizations without the need of physical exchange of the bonds. In presented experiments 30 different realizations of networks were prepared.

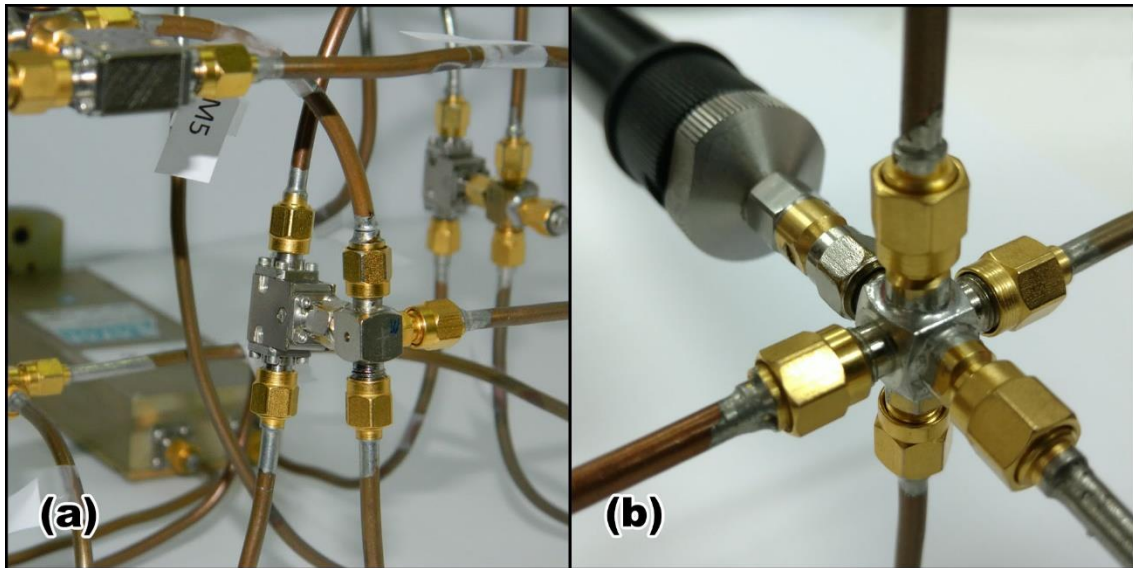


Fig. 7.2: (a) The five-arm joint which consists of the circulator and the four-arm microwave connector connected to each other. (b) The six-arm microwave connector; male connectors connected to the other vertices through microwave cables; the female connector in the middle of the photo was connected to the VNA.



Fig. 7.3: A photo of a microwave phase shifter (ATM PNR P1507D) which was used in the experiment.

In the construction of microwave networks, the coaxial cables (SMA-RG402) were used. The radius of an inner conductor of these cables (Fig 3.3) is equal to

$r_1 = 0.05$ cm, while the inner radius of the outer concentric conductor equals to $r_2 = 0.15$ cm. The dielectric constant of Teflon, which fills the space between two conductors, is equal to $\varepsilon = 2.06$. Thus, the cutoff frequency can be calculated $\nu_c \simeq \frac{c}{\pi(r_1+r_2)\sqrt{\varepsilon}} \simeq 33$ GHz. Up to this frequency only the fundamental TEM mode can propagate inside the cable, which means that the equivalence between the Schrödinger equation and the Telegraph equation still holds [79, 80]. The admissible measurement window is also limited to the technical limitations, hence, used microwave circulators PE8403 are operating in the frequency range 7 – 14 GHz. Therefore, the measurements were performed in the frequency window 7.6 – 13 GHz.

A scheme of a fully connected microwave graph composed of fifteen bonds, four phase shifters and five microwave circulators is shown in Fig. 7.1. The optical length of bonds is connected with the physical one by a simple relation $L_i^{optical} = L_i\sqrt{\varepsilon}$. In the experiment the total optical length of the microwave network was kept constant $L^{optical} \simeq 7.2$ m. It was accomplished by increasing the optical lengths of two bonds in steps of 0.112 cm, while decreasing the length of the two others by the same value.

Figure 7.4 shows an example of a reflection spectrum of a microwave network simulating a quantum graph with violated TRS. Due to absorption in the coaxial cables it exhibits weakly overlapping resonances. Therefore, loss of some resonances during the measurements is unavoidable.

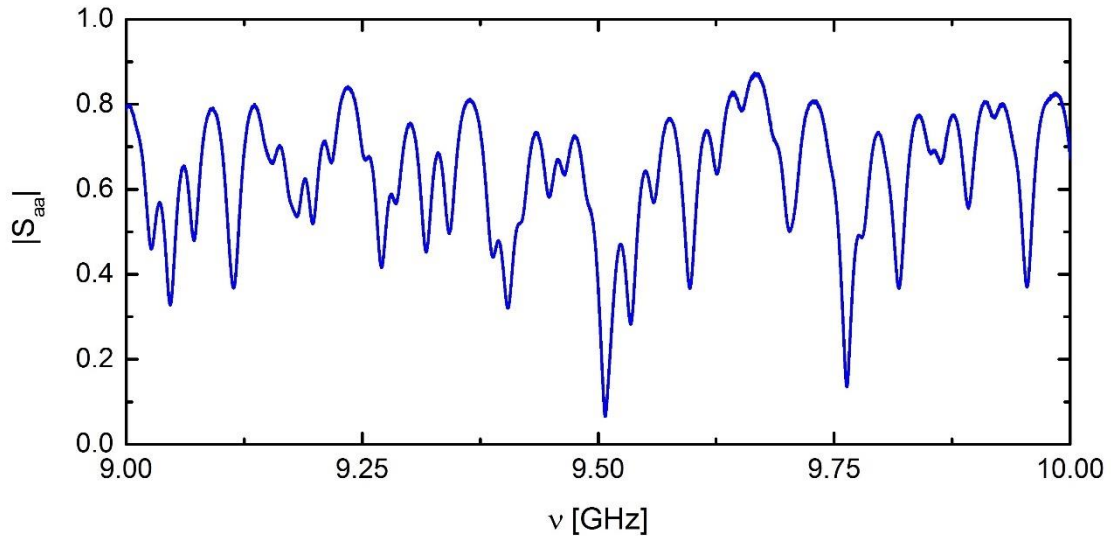


Fig. 7.4: A reflection spectrum of a microwave network with broken TRS in the frequency range 9 – 10 GHz.

By choosing lower frequency range, where overlap between the resonances are sufficiently weaker, and performing the special analysis procedure, it was possible to identify majority of eigenfrequencies. In this procedure the fluctuating part of the integrated spectral density $N^{fluc}(\nu_i)$ was investigated. The sequences of levels obtained for different realizations of the microwave networks were plotted versus the number of steps in which the lengths of four bonds was changed. At a missing or spurious eigenfrequency, the fluctuating part of the integrated spectral density exhibits jumps by more than 1. In the case of microwave networks, the application of the above procedure reduced the number of missing levels to a few percent only.

The number of resonances in a measured frequency range $\Delta\nu$, estimated on a basis of the Weyl's formula, is given in [27] by

$$\bar{N} = \frac{2L^{optical}\Delta\nu}{c}. \quad (7.1)$$

In the frequency range 7.6 – 13 GHz ~ 260 resonances are expected. However, some energy levels in experimental spectra were missing due to the resonance overlapping and small amplitudes. In the measurements we lost 4% of states. Therefore, the fraction of the observed levels was $\varphi = 0.96$.

The experimental studies of the power spectrum and the missing level statistics of the spectra characterized by the fraction of observed levels $\varphi = 0.96$ are presented in Ref. [34]. It was shown that the experimental results are in good agreement with the theoretical predictions.

For more comprehensive analysis of the spectra from the set of the measured eigenvalues, originally characterized by the fraction of observed levels $\varphi = 0.96$, 20, 35 and 50 eigenvalues were additionally randomly removed using implemented in “Matlab” function “randi”. In such a way the three new data sets were obtained which were characterized by $\varphi = 0.92$, $\varphi = 0.86$ and $\varphi = 0.81$, respectively.

Also, in this case the resonance frequencies of microwave networks needed to be unfolded to eliminate system specific properties of the spectra

$$\epsilon_i = \frac{2L}{c} \nu_i. \quad (7.2)$$

The rescaled eigenvalues ϵ_i possess the mean spacing of adjacent levels equal to unity.

For the analysis of the experimental spectra the nearest-neighbor spacing distribution $P(s)$, the number variance $\Sigma^2(L)$, the spectral rigidity $\Delta_3(L)$, and the average power spectrum $S(k)$ were used.

The results for the first sequence of data with $\varphi = 0.92$ are shown in Fig. 7.5. On all three panels black dashed line corresponds to the GUE prediction with 100% of states while black solid lines denote the GUE results obtained for the fraction $\varphi = 0.92$ of missing levels. In the case of the NNSD (panel (a)), the deviation of the theoretical curve with $\varphi = 0.92$ from the GUE prediction is small. The experimental NNSD, presented with a red histogram shows good overall agreement with the both theoretical lines due to the fact that they are very close to each other. It's extremely difficult to state from this distribution how many eigenvalues are missing and whether they were lost at all. The long-range correlation functions in turn are characterized by a greater sensitivity on the missing levels. The experimental spectral rigidity (red circles in panel (b)) lays on top of the theoretical line calculated for the fraction of observed levels $\varphi = 0.92$. The power spectrum is shown in panel (c); the experimental results (red dots) are scattered uniformly along the curve calculated for $\varphi = 0.92$.

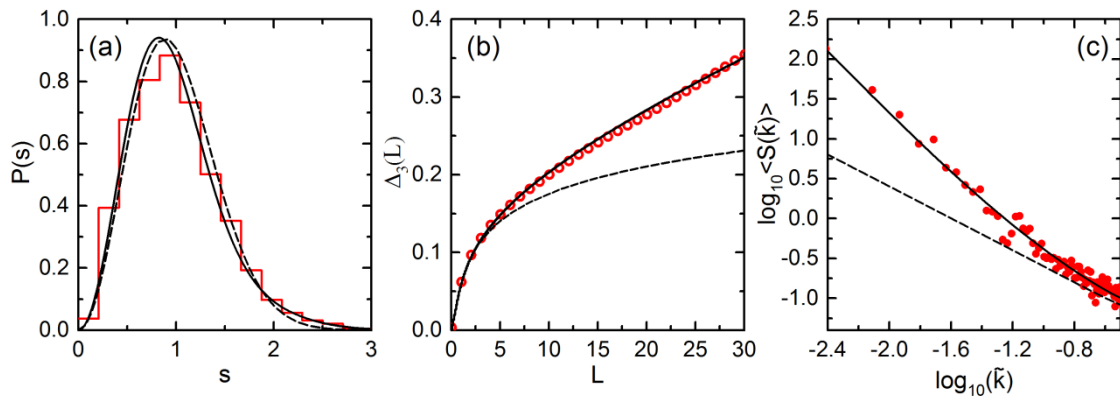


Fig. 7.5: The results obtained from the sequences of the experimental eigenvalues characterized by $\varphi = 0.92$. (a) The NNSD (red histogram). (b) The spectral rigidity (red circles). (c) The power spectrum (red dots). The black dashed lines correspond to the GUE predictions. The black solid lines correspond to the theoretical results obtained for the fraction of observed levels $\varphi = 0.92$.

The sequences of the experimental data with the fraction of observed levels $\varphi = 0.86$ were analyzed in a similar way (results shown in Fig. 7.6). The percentage

of lost states is still not big enough to draw any significant conclusions from the NNSD (panel (a)), but it becomes noticeable, that the experimental distribution (red histogram) is placed a little bit to the left of the GUE prediction. Both the Dyson-Mehta statistic (red circles in panel (b)) and the power spectrum (red dots in panel (c)) show good agreement with the corresponding theoretical lines.

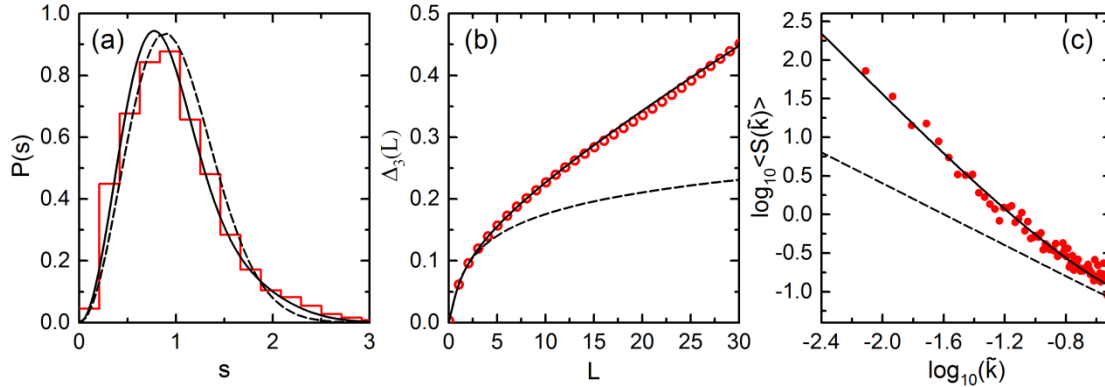


Fig. 7.6: The results obtained from the sequences of the experimental eigenvalues characterized by $\varphi = 0.86$. (a) The NNSD (red histogram). (b) The spectral rigidity (red circles). (c) The power spectrum (red dots). In all three panels black dashed lines correspond to the GUE predictions. The black solid lines correspond to the theoretical results obtained for the fraction of observed levels $\varphi = 0.86$.

The last set of experimental data was characterized by the largest amount of lost levels, $\varphi = 0.81$. Now, when the amount of missing levels has risen it is possible to say with certainty, that experimental NNSD (red histogram in Fig. 7.7(a)) departs from the GUE prediction. Similarly to previous situations, the long-range correlations, namely, the spectral rigidity (red circles in panel (b)) and the power spectrum (red dots in panel (c)) show very good agreement with the theoretical predictions for $\varphi = 0.81$.

To compare all three cases side to side, the integrated nearest-neighbor spacing distribution $I(s)$ and the number variance $\Sigma^2(L)$ have been used. The integrated NNSD for the microwave networks is shown in Fig. 7.8(a). Empty red circles correspond to $\varphi = 0.92$, empty blue diamonds to $\varphi = 0.86$ and empty green triangles to $\varphi = 0.81$. It is visible that in the case of the integrated NNSD the experimental points

are congested along the GUE curve showing that the integrated NNSD is not particularly sensitive to missing levels.

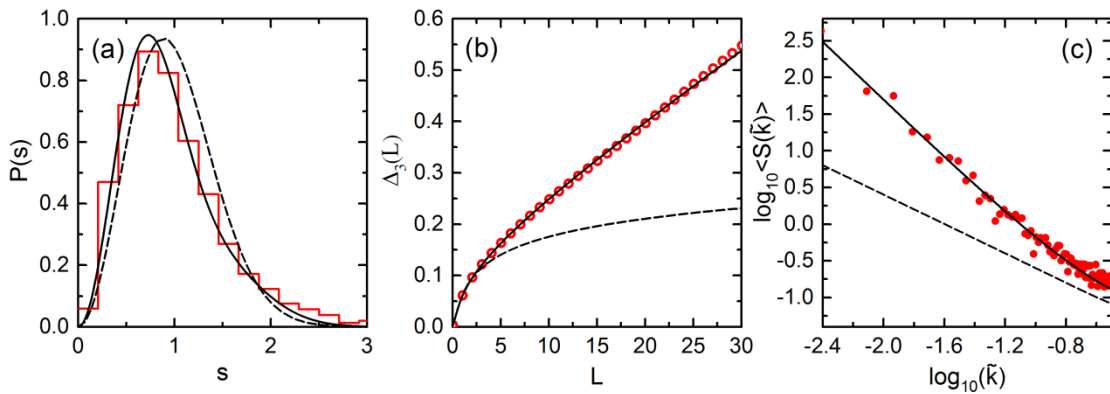


Fig. 7.7: The results obtained from the sequences of the experimental eigenvalues characterized by $\varphi = 0.81$. (a) The NNSD (red histogram). (b) The spectral rigidity (red circles). (c) The power spectrum (red dots). In all three panels black dashed lines correspond to the GUE predictions. Black solid lines correspond to the theoretical results obtained for the fraction of observed levels $\varphi = 0.81$.

The number variance for all tree sequences of experimental data, characterized by $\varphi = 0.92$, $\varphi = 0.86$ and $\varphi = 0.81$, is shown in Fig. 7.8(b) as red circles, blue diamonds and green triangles, respectively. Each experimental distribution is compared to the theoretical one, black dash dot line for $\varphi = 0.92$, black short dash line for $\varphi = 0.86$ and black dash line for $\varphi = 0.81$, respectively. The GUE prediction is marked with black solid line. It is clearly visible that for all three experimental sequences of data, the number variance is in good agreement with the appropriate theoretical prediction.

The inspection of the results reveals, that the NNSD and the integrated NNSD can provide information about lost states only in the case of large fraction of missing levels, but their accuracy leaves much to be desired. In cases where the number of missing states is small and a better precision is required, the best option is to use the long-range correlations. The power spectrum provides a particularly useful statistical measure, especially in the presence of missing levels. The agreement between the modified

experimental data and the analytical formulas for all these statistical measures clearly shows the potential of incomplete spectra analysis.

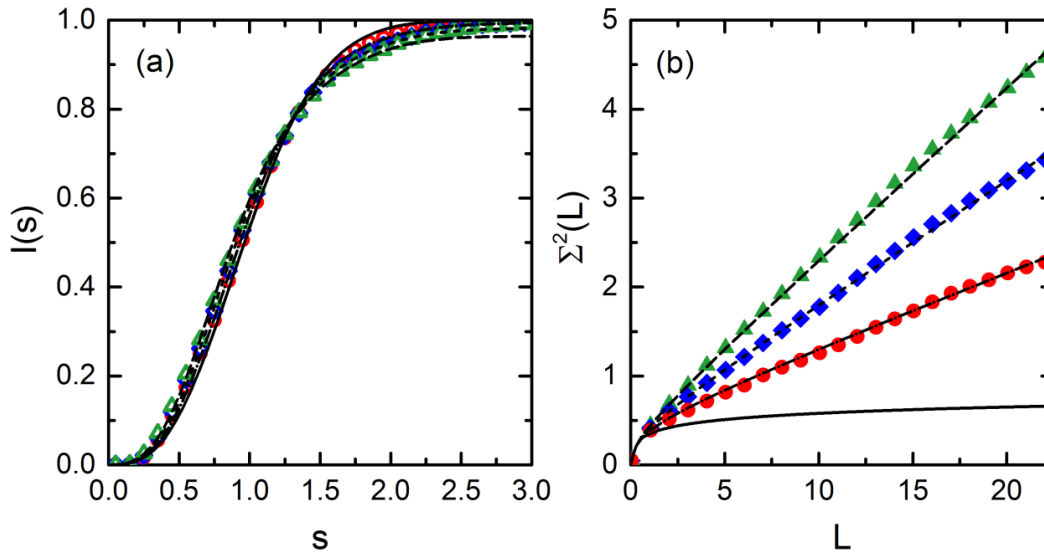


Fig. 7.8: (a) The integrated NNSD (b) The number variance. The results are obtained for three sequences of the experimental data characterized by $\phi = 0.92$, $\phi = 0.86$ and $\phi = 0.81$, respectively. The detailed description is presented in the text.

7.2. Missing level statistics of microwave networks with preserved TRS

The experimental and numerical studies of the systems with broken TRS that considered missing states were supplemented by the studies of the systems with preserved TRS [36, 48, 81, 82]. Quantum graphs with chaotic classical dynamics and preserved time-reversal symmetry are generally believed to provide an ideal basis for the experimental study of problems originating from the field of quantum chaos and random matrix theory. However, non-universality in the spectral properties of time-reversal invariant microwave networks and quantum graphs causes the deviations in the long-range correlations. There is an assumption, that they can be attributed to the occurrence of the shortest periodic orbits. Such orbits explore only the individual bonds of a graph and, as a result, do not sense the chaoticity of its dynamics [83]. It is expected that in the case of networks with broken time reversal symmetry possessing directed bonds, the influence of short periodic orbits into the level statistics should be much less pronounced. This suspicion is traced from the results obtained in the previous

section. In the following investigations the short- and long-range correlations for microwave networks with preserved TRS based on missing level statistic will be presented and compared with previously obtained results.

To complete the experimental studies the microwave hexagon fully connected network possessing TRS was constructed. All vertices with the exception of one were five-arm joints. The last one had an additional arm which allowed to connect the graph to the VNA (Fig. 6.1). As in the previous graph, the coaxial cables SMA-RG402 were used. The lengths of four bonds were changed in steps of ± 0.42 cm using the phase shifters (Fig. 7.3). By changing the lengths of the specific bounds, an ensemble of 30 different networks with the same total optical length $L^{optical} \simeq 7.2$ m was created. Each coaxial cable's optical length, including their extensions across the junctions, was measured separately and then summed up in order to get the total length. The lengths of the cables were chosen in such a way that the microwave networks simulated quantum graphs with chaotic dynamics. The scheme of the six-vertex fully connected microwave network with preserved TRS is shown in Fig. 7.10. As previously, the one-port scattering matrix S , presented with Eq. (6.1), was measured.

Figure 7.9 shows a reflection spectrum of a microwave network possessing TRS in the frequency range from 2–3 GHz. The positions of the resonances yield the eigenfrequencies and thus the eigenvalues of the corresponding quantum graph. Ohmic losses in the coaxial cables lead to a broadening of the resonances. At low frequencies, thereby arising overlaps between the resonances were sufficiently weak.

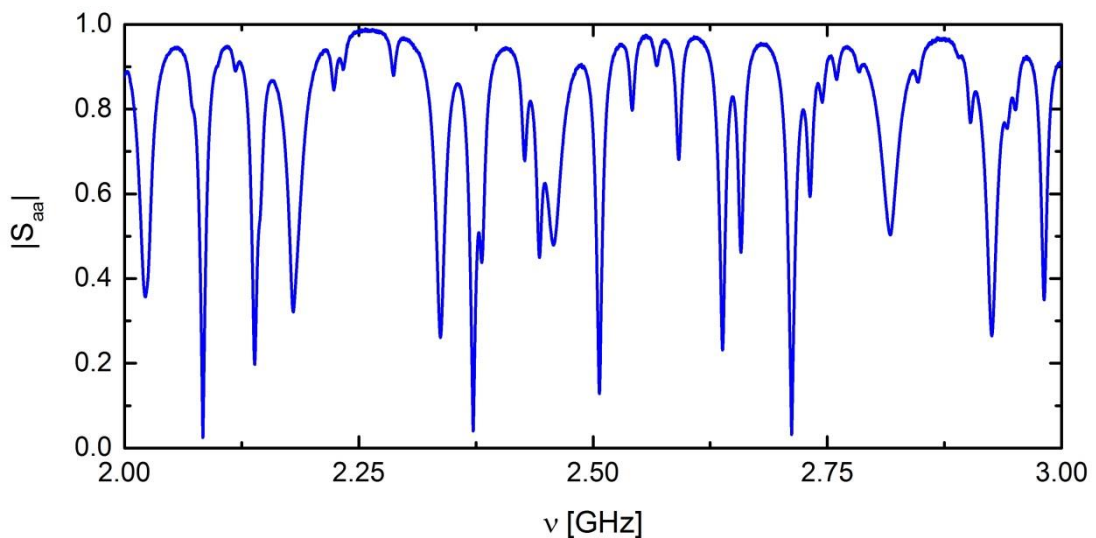


Fig. 7.9: A sample of the reflection spectrum of a microwave network with preserved TRS in the frequency range 2–3 GHz.

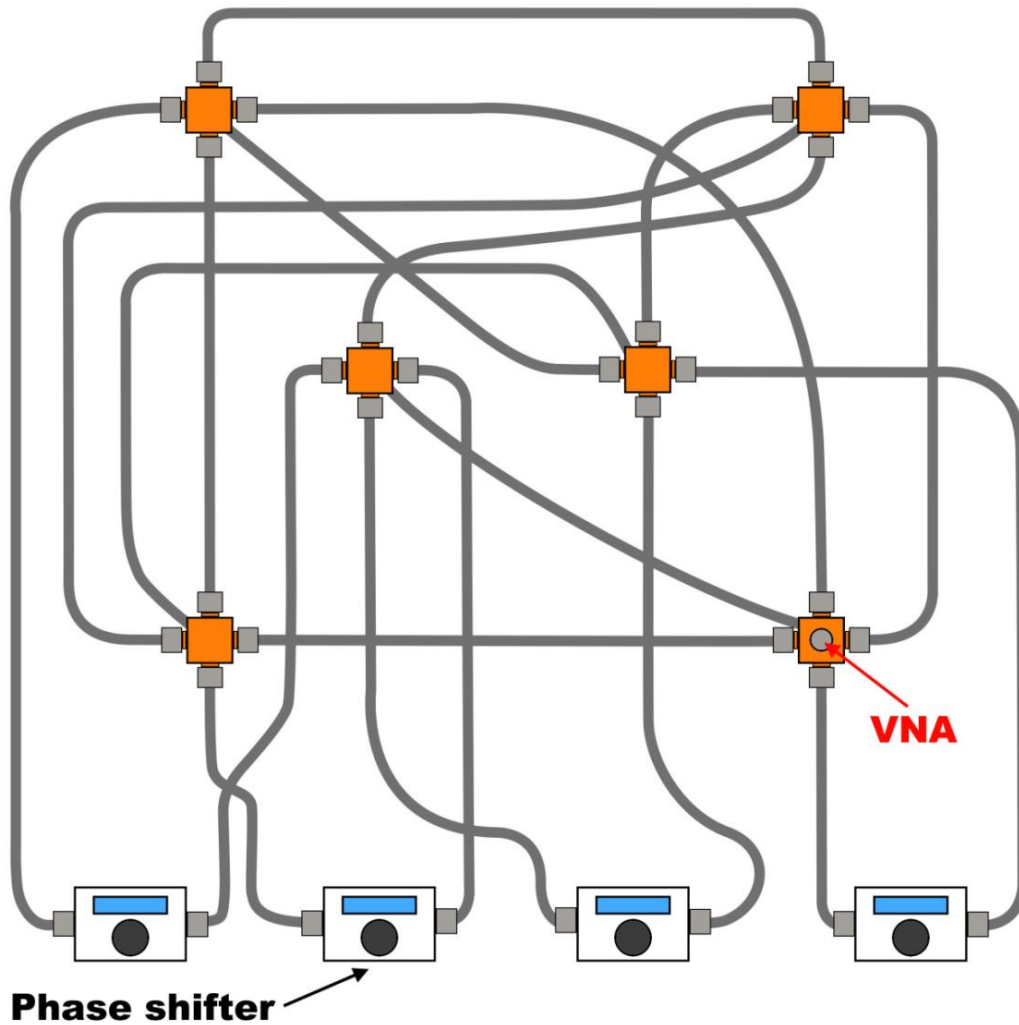


Fig. 7.10: A scheme of the six-vertex fully connected microwave network with preserved TRS. The VNA is connected to vertex marked “VNA”. The optical lengths of four bounds were changed with the phase shifters. The lengths of two of them were increasing while the lengths of the other two were decreasing by the same amount.

At this point it is already evident that the impact of missing levels on the spectral fluctuations is particularly large for long-range spectral fluctuations. The same statistical measures as before were used [45]. The measurements were performed in the frequency window 1 – 5.5 GHz. Approximately 200 eigenfrequencies were identified for each network, yielding the fraction of observed levels $\varphi = 0.92$. The measured spectra were rescaled (unfolded) in accordance to the Weyl’s law, exactly like in the previous case. The experimental distributions were generated by computing the

averages of the corresponding spectral correlations obtained for each realization of microwave networks. The missing level statistics for microwave networks with preserved TRS are shown in Figures 7.11 and 7.12. The distribution of the spacing between adjacent eigenvalues and its integrated form is shown in Fig. 7.11(a) with a red histogram and Fig. 7.11(b) with red diamonds, respectively. Both statistics seem to coincide well with the GOE theoretical curve (black dashed line). A small percentage of lost states does not significantly affect the distributions. Black solid lines correspond to the numerical calculations that took into account 8% of missing states ($\varphi = 0.92$).

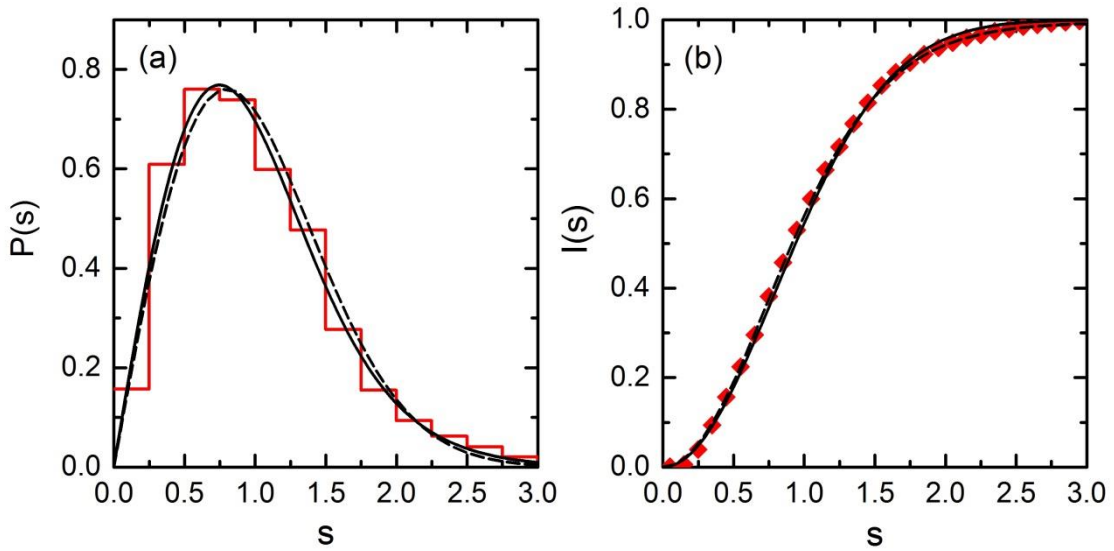


Fig. 7.11: The short-range spectral fluctuations calculated for the experimental spectra of the microwave networks possessing TRS. (a) The NNSD (red histogram). (b) The integrated NNSD (red diamonds). Black dashed lines correspond to the GOE predictions. Black solid lines correspond to the theoretical results obtained for the fraction of observed levels $\varphi = 0.92$.

I also calculated the long-range spectral fluctuations such as the number variance $\Sigma^2(L)$ and the power spectrum. The number variance is shown in Fig. 7.12(a) with red triangles. The power spectrum is demonstrated in Fig. 7.12(b) as red dots. Both distributions clearly depart from the GOE distributions (black dashed line in both panels). However, they are very well described by the theoretical curves obtained using the formulas (5.10) and (5.11) (dark solid lines). This observation is very interesting because in Ref. [83] it was demonstrated that in the case of GOE networks the power

spectrum for the complete spectra departure from the GOE prediction. This phenomenon may be attributed to the occurrence of short periodic orbits confined to individual bonds. Thus, the missing levels in the GOE spectra improve the agreement of the experimental power spectrum with the theoretical one.

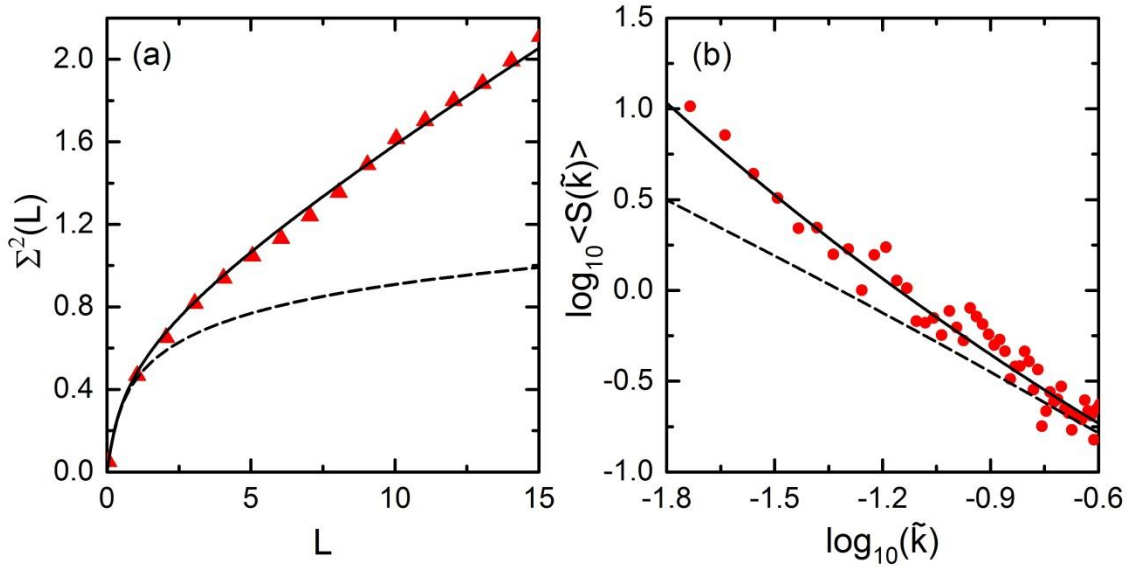


Fig. 7.12: The long-range spectral fluctuations calculated for the experimental spectra of the microwave networks possessing TRS. (a) The number variance (red triangles) (b) The power spectrum (red dots). Black dashed lines correspond to the GOE predictions. Black solid lines correspond to the theoretical results obtained for the fraction of observed levels $\varphi = 0.92$.

In the both GOE and GUE cases the experimental results are in good agreement with the analytical expressions for missing level statistics that explicitly consider the fraction of observed levels φ . The power spectrum appeared to be especially useful in the description of incomplete spectra of quantum systems with violated and preserved time invariance. The incomplete spectra is an important problem one has to cope with in real physical systems like, e.g. nuclei and molecules [84-87], so such a procedure is indispensable for their analysis.

CHAPTER 8

MISSING-LEVEL STATISTICS OF THE THREE-DIMENSIONAL CHAOTIC MICROWAVE CAVITIES

Low-dimensional microwave systems are extremely rich and therefore can be successfully used for the experimental investigations of the properties of quantum systems that exhibit chaotic dynamics in the classical limit. Unlike the one-dimensional (1D) microwave networks [4, 18, 19] and the two-dimensional (2D) microwave cavities [38, 39, 41, 88-91] simulating quantum graphs and 2D billiards, respectively, the three-dimensional (3D) microwave cavities do not have quantum counterparts. This is connected with the fact that in the case of 3D microwave cavities there is no direct analogy between the Schrödinger equation and the vectorial Helmholtz equation. As follows, generally one cannot use 3D cavities to simulate 3D quantum systems. However, it was shown experimentally by Deus et al. [92] that the distribution of eigenfrequencies of the 3D chaotic (irregular) microwave cavity displays behavior characteristic for classically chaotic quantum systems, viz. the Wigner distribution of the nearest-neighbor spacings. These findings indicate that 3D chaotic microwave cavities can be used in the investigation of the properties of wave chaos.

In the spectral measurements of any systems the loss of some resonances is inevitable. It may be caused by low signal-to-noise ratio, by degeneration or overlap of resonances due to losses (absorption/system openness). In the case of 3D systems we have an additional obstacle: a large density of states. However, one should mention that in the studies of spectral statistics of acoustic resonances in 3D aluminum [93] and quartz [94] blocks, characterized by high quality factors factors $Q \approx 10^4 - 10^5$, no missing resonances were reported. In billiard systems, even higher quality factors were obtained in the experiments with superconducting microwave cavities [95]. In normal conducting resonators the quality factors are much lower ($Q \approx 10^3$) and the loss of some modes is either very likely or even inevitable, therefore, in the recent studies of

such a chaotic 3D microwave cavity the missing levels were explicitly taken into account [96-97].

The determination of the system chaoticity and symmetry class defined in RMT using its spectral properties requires knowledge of complete series of eigenvalues, so experimentally it is generally a difficult task [98-101]. The procedures developed for microwave networks with broken [34] and preserved [83] TRS (chapters: 7.1 and 7.2) show that this is possible provided that several statistical measures, e.g. a short-range correlation function (the nearest-neighbor spacing distribution - NNSD), long-range correlation functions (e.g., the spectral rigidity), and the power spectrum of level fluctuations [49, 50, 66] will be analyzed.

In the experimental studies of 3D systems we used the 3D microwave cavity. The overall view of the experimental setup is shown in Fig. 8.1. The 3D microwave cavity was made of polished aluminum type EN 5754 and consists of four elements. The rough semicircular element of height 60 mm (marked by (1) in Fig. 8.1) is closed by three flat parts: side (labeled by (2) in Fig. 8.1) and upper ones labeled (3) and (4). The bottom element is a slightly inclined and convex plate (labeled by (3) in Fig. 8.1) preventing the appearance of bouncing balls orbits between the upper and lower walls of the cavity. The radius function $R(\theta) = R_0 + \sum_{m=2}^M a_m \sin(m\theta + \Phi_m)$, where the mean radius $R_0 = 10.0$ cm, $M = 20$, a_m , and Φ_m are uniformly distributed on $[0.084, 0.091]$ cm and $[0, 2\pi]$, respectively, and $0 \leq \theta < \pi$, described the rough, semicircular element on the plane of the cross-section. An aluminum scatterer inside the cavity, mounted on the metallic axle in its upper wall (see Fig. 8.1) was used to realize various cavity configurations. The orientation of the scatterer was changed by turning the axle around in 18 identical steps, each equal to $\pi/9$. Besides the hole for the scatterer in the bottom wall there are three other holes A_1 , A_2 , and A_3 for antennas.

An vector network analyzer (VNA) (Fig 6.1) was used to perform two-port measurements of the four-element scattering matrix Eq. (4.27). The measurements were done in the frequency range 6 – 11 GHz for all three combinations of the antennas positions. The antennas penetrated 6 mm into the cavity with a wire of 0.9 mm in diameter. The “third” empty hole was plugged by brass plug during the measurement. Previous measurements [102] have shown that the total absorption of the cavity is mainly related to internal absorption which is much greater than that associated with antennas/channels.

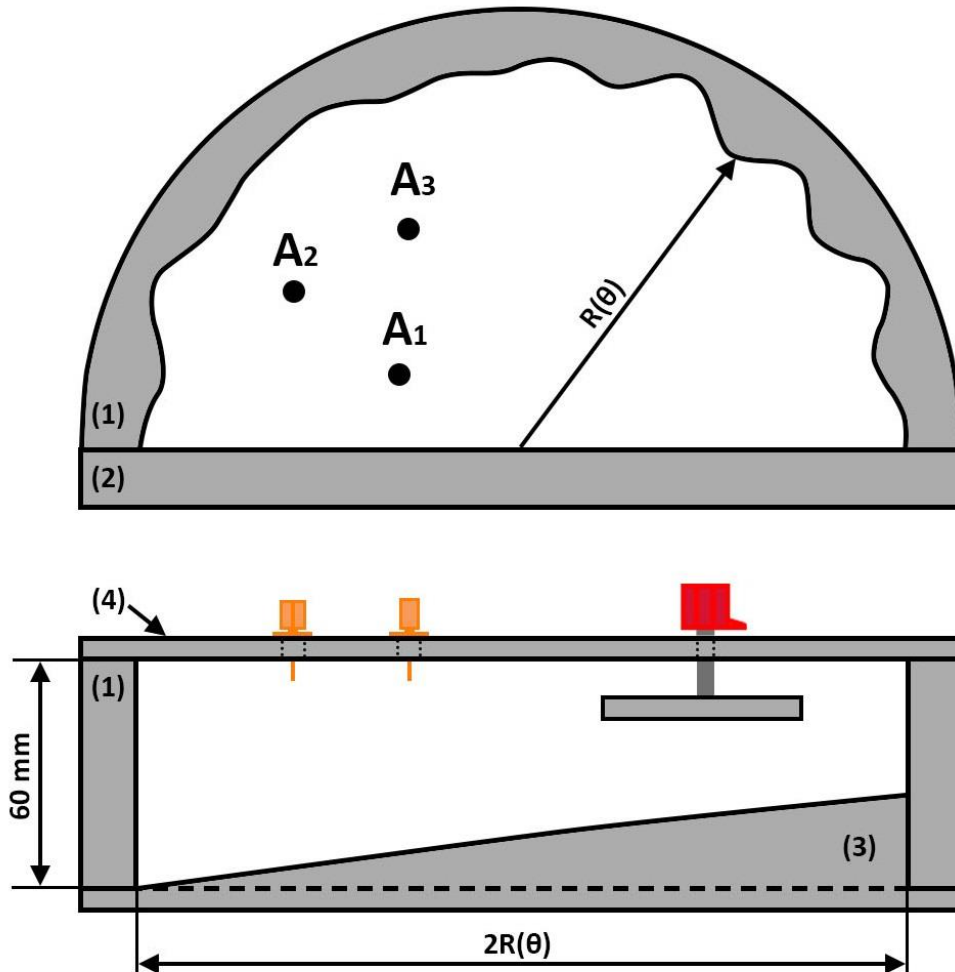


Fig. 8.1: A sketch of the 3D cavity on the cross-section plane (see the detailed description in the text). The scatterer is located on the right side inside the cavity. The antennas are marked with yellow color.

Fig. 8.2 shows the examples of the modules of the reflected $|S_{aa}|$, $|S_{bb}|$, and transmitted $|S_{ab}|$ signals measured in the lowest 6 – 7 GHz and highest 10 – 11 GHz frequency ranges. In the low frequency range, when the resonances are well separated, comparing the spectra $|S_{aa}|$ and $|S_{bb}|$, it is clearly seen that the number of the detected resonances may depend on the position of the antenna. The transmission signal $|S_{ab}|$ can be also used in the search for the resonances, however, even for this low frequency range not all resonances are separated and visible. In turn, in the higher frequency range, due to the cubic dependence of the number of resonances on the frequency, the overlapping resonances have appeared. Therefore, losing resonances in the measurements is inevitable.

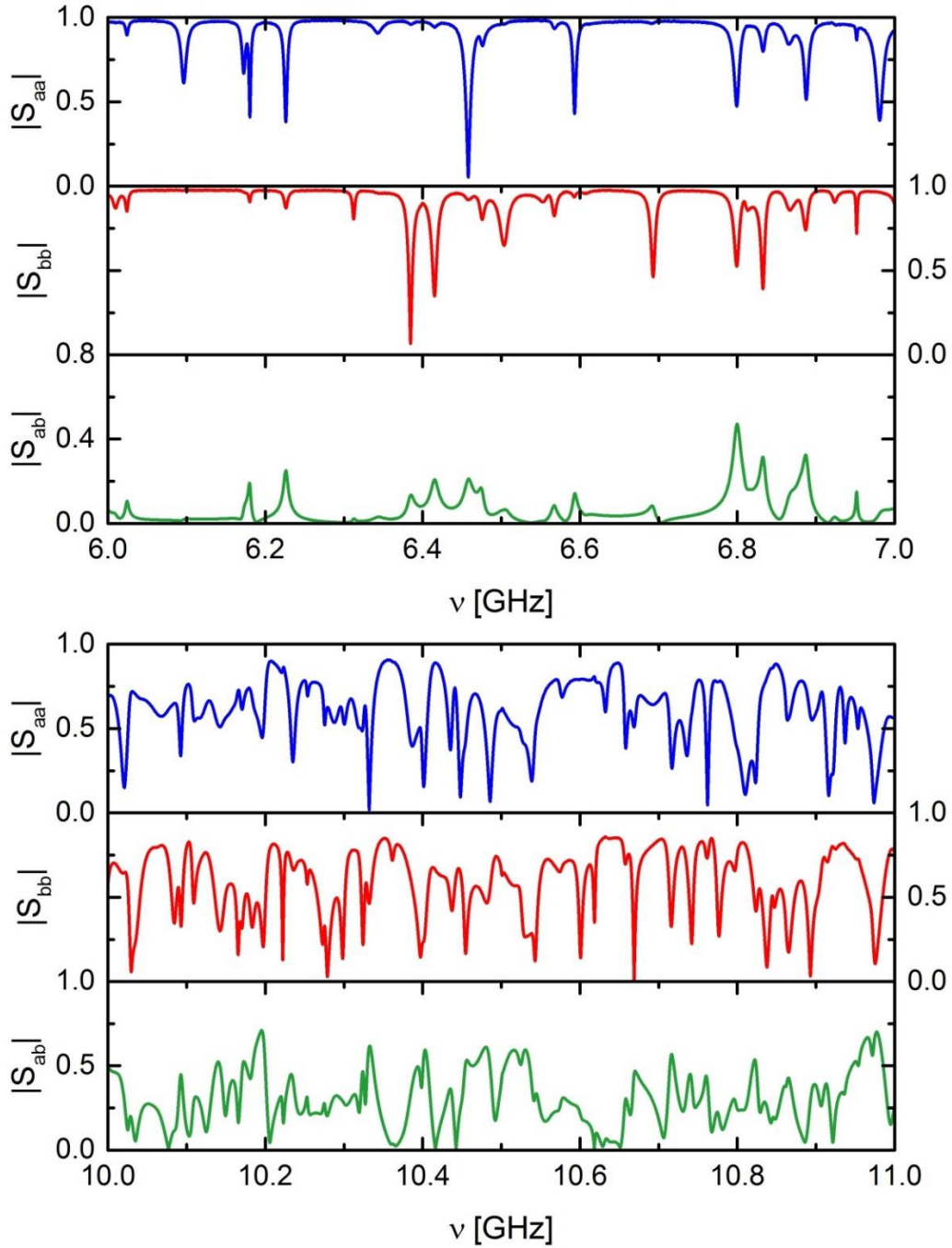


Fig. 8.2. Examples of the measured modules of the elements $|S_{aa}|$, $|S_{bb}|$ and $|S_{ab}|$ of the scattering matrix \hat{S} of the 3D microwave cavity in the frequency range 6 – 7 GHz and 10 – 11 GHz, respectively.

In order to analyze the experimental data specific features of the studied system was eliminated by the rescaling procedure $\epsilon_i = N(\nu_i)$. In the case of the 3D microwave cavities it was carried out using the Weyl formula [103-106]

$$N(\nu) = A\nu^3 - B\nu + C. \quad (8.1)$$

The coefficient $A = \frac{8\pi}{3c^3}V$, where c is speed of light in vacuum and $V = (7.267 \pm 0.012) \times 10^{-4} \text{ m}^3$ is the volume of the cavity reduced by the volume of the scatterer. The dependent on the surface of a cavity a term proportional to v^2 disappears due to boundary conditions of the electromagnetic field in the conducting cavity walls [104]. The coefficient B depends on the surface curvature, internal angles, and the edge length of the cavity [103]. The constant C is also associated with the shape of the cavity and in the simple case of the cubic cavity $C = \frac{1}{2}$ [105]. The coefficients B and C are generally difficult to determine exactly, so fitting procedures are necessary to obtain the cumulative number of levels $N(\nu)$ for 3D irregular cavities.

In order to analyze the data, I will use the nearest-neighbor spacing distribution, the integrated nearest-neighbor spacing distribution $I(s)$, the spectral rigidity of the spectrum and the power spectrum.

In the systems with losses, when the problem of missing levels may be very severe, the fluctuations of the scattering matrix elements can be useful. The correlation functions [60, 77], the Wigner's reaction matrix and the elastic enhancement factor [19, 107] are sensitive measures of system chaoticity, however don't provide any information about missing energy levels.

In Figs. (8.3) and (8.4) the experimental results obtained in the frequency range 6 – 11 GHz for 30 realizations of the cavity are presented. The number of the detected resonances depends on the cavity realization, therefore, from each cavity spectrum a small number of resonances has been randomly removed to obtain the same number $\Delta N_{exp} = 208$ for all cavity configurations. The NNSD and the integrated NNSD, shown in Fig 8.3(a) and Fig 8.3(b), while the spectral rigidity and the power spectrum are shown in Fig 8.4(a) and Fig 8.4(b), respectively. The dashed (black) line denotes the theoretical predictions for the complete spectra $\varphi = 1$ of the GOE system. Ten terms of Eq. (5.1) was used in the numerical calculation of the NNSD. Experimental data are represented by a red histogram and red full diamonds in Fig. 8.3 panels (a), (b) and red circles and dots in Fig. 8.4 panels (a), (b). Using the equations for the spectral rigidity (5.9) and the power spectrum (5.11) it was found that the best agreement between the theoretical predictions for incomplete spectra (dark solid line) and experimental results occurs for $\varphi = 0.85$, as shown in panels (a) and (b) of Fig. 8.4. In turn, $\varphi = 0.85$ was inserted into equations (5.1) and (2.25) to calculate the NNSD and the INNSD which are shown in Fig. 8.3 panels (a) and (b). It is easily seen that the spectral rigidity and the

power spectrum are much more sensitive measures of losing states than the nearest-neighbor spacing distribution. The excellent agreement between the theoretical predictions for incomplete spectra and the experimental results shows that the investigated system, 3D irregular cavity, belongs to systems characterized by preserved TRS (GOE) and that the resonances have been randomly lost.

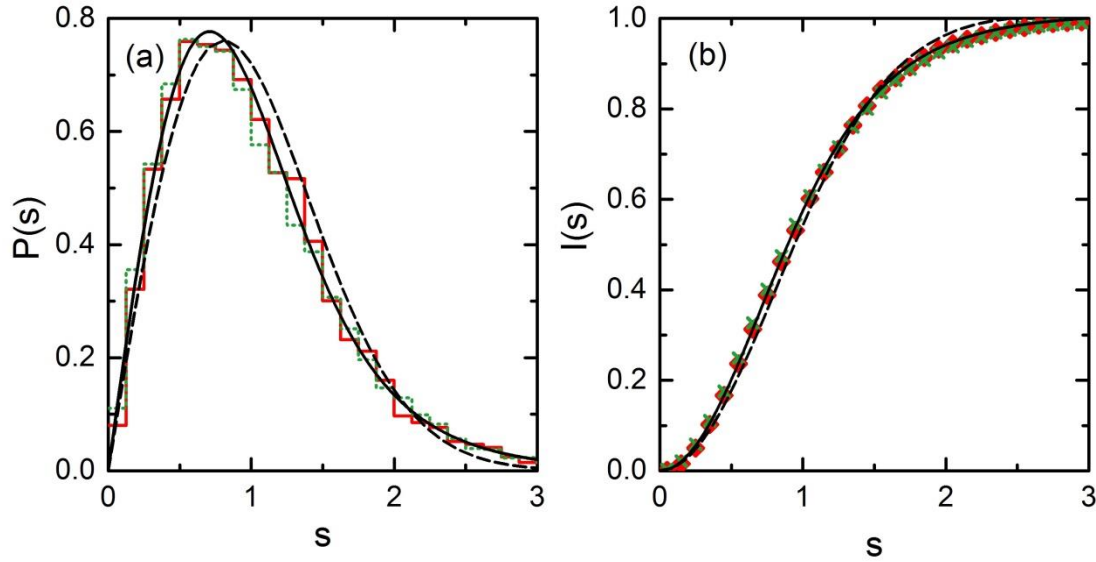


Fig. 8.3: The spectral properties of the rescaled resonance frequencies of the 3D microwave cavity. (a) The experimental results for the NNSD (red histogram) compared with the NNSD obtained from the eigenvalues of the random matrices (green dotted histogram). (b) The experimental results for the integrated NNSD (red diamonds) compared with the integrated NNSD obtained from the eigenvalues of the random matrices (green crosses). Black dashed lines correspond to the GOE predictions. Black solid lines correspond to the theoretical results obtained for the fraction of observed levels $\varphi = 0.85$.

In order to estimate the theoretical number of resonances ΔN_{theo} in the frequency range 6 – 11 GHz, which is required for the calculation of φ , nine configurations of the cavity complete spectra in the frequency range 7 – 9 GHz were used [96]. The analysis done by M. Białous allowed to make the fits of the experimental staircase functions to the formula (8.1) with the fixed coefficient $A = (0.2259 \pm 0.0004) \cdot 10^{-27} \text{s}^3$. The fits gave the average values of the coefficients $B = (1.442 \pm 0.174) \cdot 10^{-9} \text{s}$ and

$C = -66.0 \pm 1.4$. Then using the formula (8.1) the theoretical number of resonances $\Delta N_{theo} = 245$ in the frequency range 6 – 11 GHz was evaluated.

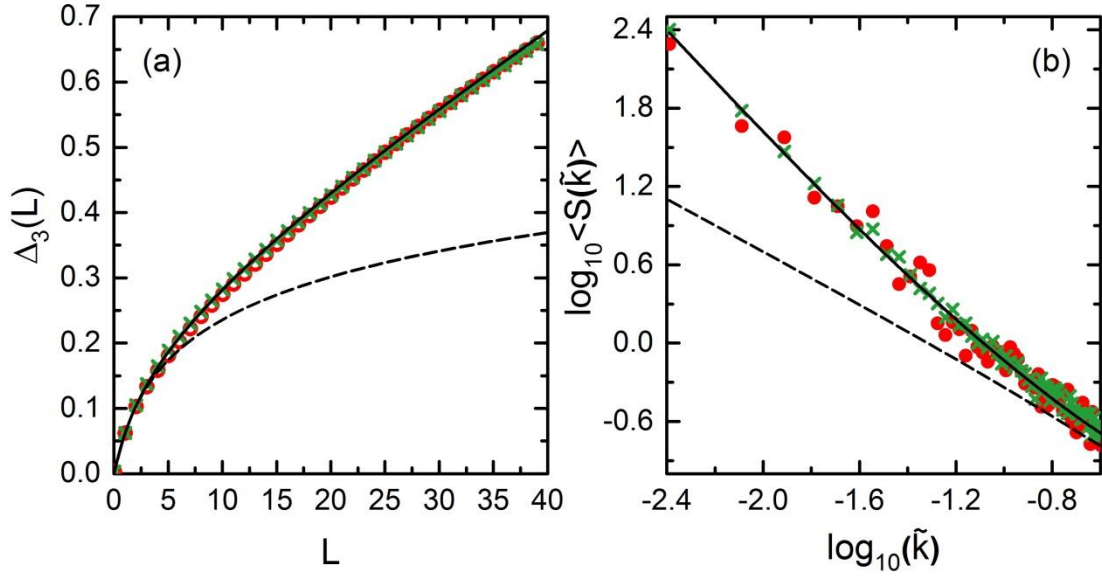


Fig. 8.4: (a) The spectral rigidity of the experimental spectra (red circles) are compared to the spectral rigidity of the eigenvalues of the random matrices (green crosses) (b) The average power spectrum of the level fluctuations of the experimental spectra (red dots) are compared to the power spectrum of the eigenvalues of the random matrices (green crosses). Black dashed lines correspond to the GOE predictions. Black solid lines correspond to the theoretical results obtained for the fraction of observed levels $\varphi = 0.85$.

The fraction of the detected levels $\varphi = 0.85$ estimated from the missing-level statistics (Eqs. 5.9 and 5.11) can now be compared with the fraction $\frac{\Delta N_{exp}}{\Delta N_{theo}} = \frac{208}{245} \approx 0.849$ obtained as a ratio of the experimentally found eigenfrequencies and those predicted from the Weyl formula in the frequency range 6 – 11 GHz.

The discussed above theoretical and experimental results are additionally compared to the numerical results obtained directly by the application of the random matrix theory. I created 99 realizations of random, real symmetric matrices of a size $N = 295$, representing GOE system. 20 eigenvalues of the matrix were removed from the beginning and the end of each set of eigenvalues, yielding 245 eigenvalues as for the complete spectrum. Then, 15% of the eigenvalues were randomly removed, so I finally

got 208 eigenvalues as it was the experiment, which were rescaled using a fifth order polynomial. The results for all considered measures are also presented in Figs. 8.3 and 8.4. The NNSD is marked by a green dotted histogram, while the integrated NNSD, the spectral rigidity and the power spectrum by green crosses. Again, the agreement with the experimental results is remarkable, confirming that the investigated system, 3D irregular cavity, belongs to the systems with preserved time reversal symmetry and that the resonances have been randomly lost.

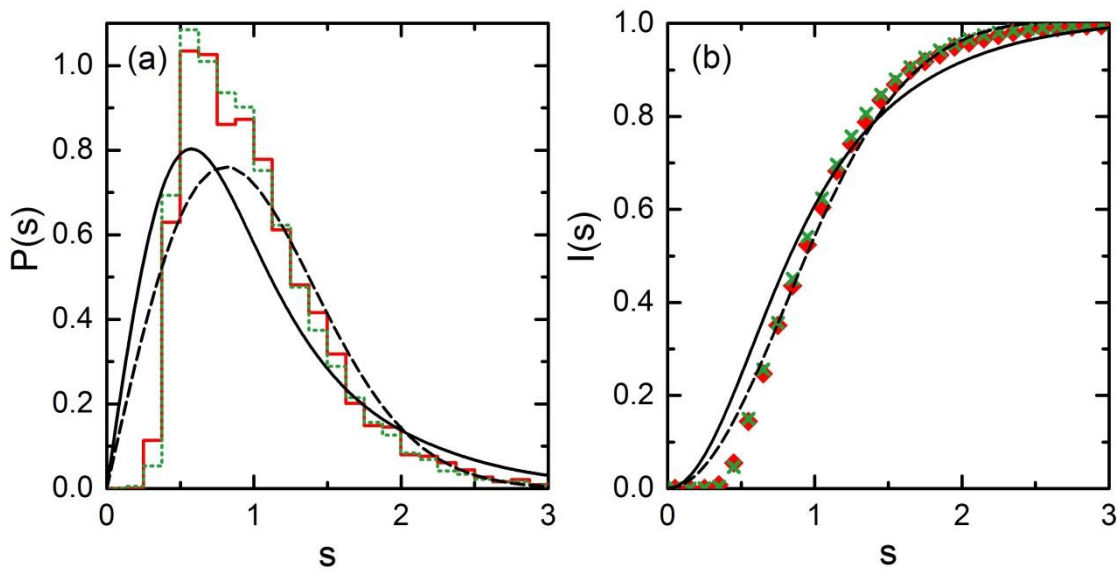


Fig. 8.5: The spectral properties of the rescaled eigenvalues of the 3D microwave cavity calculated for the modified experimental spectra from which the closest resonances were removed. (a) The experimental results for the NNSD (red histogram) compared with the NNSD obtained from the eigenvalues of the random matrices (green dotted histogram). (b) The experimental results for the integrated NNSD (red diamonds) compared with the integrated NNSD obtained from the eigenvalues of the random matrices (green crosses). Black dashed lines correspond to the GOE predictions. Black solid lines correspond to the theoretical results obtained for the fraction of observed levels $\varphi = 0.65$.

From the experimental point of view, it is important to analyze a more complicated situation when some of the resonances are not randomly lost, e.g., due to forming the clusters. For that reason, I modified the experimental spectra, originally

with 15% of randomly missing levels, using the following procedure. In the step by step procedure in an analyzed spectrum I identified the pair of resonances, the least distant from each other, and eliminated one of them until I reached $\varphi = 0.65$. In this way I additionally removed 20% of resonances due to clustering. In Figs. 8.5 and 8.6 the results for the modified experimental spectra (red symbols) are compared with the results of RMT calculations (green symbols), the GOE prediction for the complete spectra (black dashed lines) and the predictions for the missing-level statistics (Eqs. (2.25), (5.1), (5.9), and (5.11)) calculated for $\varphi = 0.65$ (black full lines).

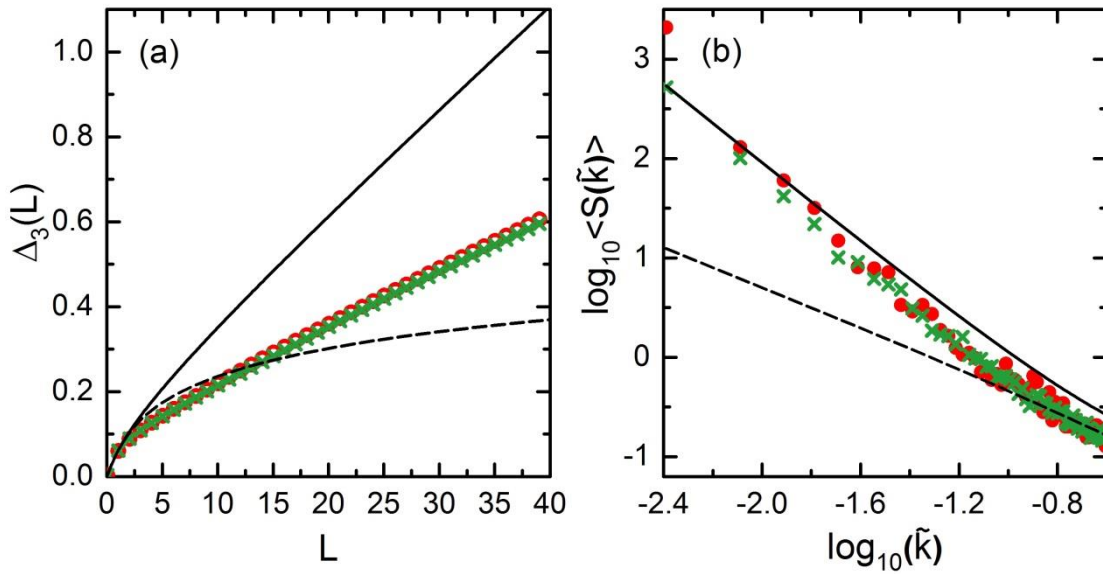


Fig. 8.6: (a) The spectral rigidity of the modified experimental spectra, from which the closest resonances were removed (red circles), are compared to the spectral rigidity of the eigenvalues of the random matrices (green crosses). (b) the average power spectrum of the level fluctuations of the modified experimental spectra, from which the closest resonances were removed (red dots), are compared to the power spectrum of the eigenvalues of the random matrices (green crosses). Black dashed lines correspond to the GOE predictions. Black solid lines correspond to the theoretical results obtained for the fraction of observed levels $\varphi = 0.65$.

It is clearly visible that the missing level statistics (black solid lines in all panels) fail in the description of the spectra in which the resonances were not randomly lost (red full line histogram in Fig. 8.5(a), red full diamonds in Fig. 8.5(b), red circles in

Fig. 8.6(a), red dots in Fig. 8.6(b)). This is an important finding because the loss of energy levels due to their degeneration or overlap caused by absorption or openness of a system is very common.

The results of RMT calculations (green dotted histogram in Fig. 8.5(a), green crosses in Fig. 8.5(b), Fig. 8.6(a) and Fig. 8.6(b)) in which the procedure of eliminating eigenvalues mimic the procedure used for the experimental data are in good agreement with experimental ones. It should be pointed out that these numerical calculation are sensitive to the order in which the eigenvalues are deleted. The results may slightly vary depending whether the procedure of the deletion starts from the overlapping resonances or from the random ones.

Summarizing, in this chapter I extended the analysis of missing level statistics, so successfully applied in the case of 1D systems (Chapter 7), to the 3D ones. I analyzed the two important cases in the missing level analysis: the situation of randomly lost resonances and the situation when an additional fraction of resonances is omitted due to their clustering (overlapping). In the case of randomly missing resonances the results are in agreement with the level-missing statistics. However, in the case of many overlapping resonances the direct random matrix theory calculations are required to properly simulate the experimental results.

CHAPTER 9

CONCLUSIONS

In the presented thesis I investigated the manifestation of classically chaotic dynamics in properties of the corresponding quantum or, more generally, wave-dynamical systems. The elastic enhancement factor W and the power spectrum $S(k)$, characterized by $1/f^\alpha$ noise dependence, were of primary interest in these investigations. Despite the fact that initially low-dimensional wave structures were main targets, the 3D cavity resonators were also considered.

The conducted experimental and theoretical investigations included the study of the nearest-neighbor spacing distribution, its integrated form, the spectral rigidity, the number variance, the power spectrum of level fluctuations, and the elastic enhancement factor in the microwave structures. Quantum systems were simulated with 1D and 2D wave structures by exploiting formal analogy of the 1D Schrödinger equation and the Telegraph equation and the 2D Schrödinger equation and the Helmholtz equation, respectively. The 3D microwave systems do not have quantum counterparts, thus, they were used for the investigation of wave chaos.

It was shown that the elastic enhancement factor W is a useful measure of internal chaos in 2D quantum systems in a presence of moderate absorption. The results obtained for the rectangular cavity displayed a transition from regular to chaotic motion. Moreover, the numerical calculations confirmed this interpretation showing that this system is characterized by different from zero chaoticity parameter $k = 2.8$. The elastic enhancement factor W measured for the microwave rough cavity displayed behavior characteristic for quantum chaotic systems.

The fluctuation properties in incomplete spectra of microwave networks simulating chaotic quantum graphs with broken and preserved time reversal symmetry were studied numerically and experimentally. The microwave networks, characterized by the GUE symmetry possessing missing levels, were studied experimentally for the first time. The obtained results are in good agreement with the analytical expressions that explicitly take into account the fraction of observed levels φ . The power spectrum $S(k)$ turned to be particularly sensitive to it. It was demonstrated that the power

spectrum in the combination with short- and long-range spectral fluctuations provides a powerful tool for the determination of the fraction of randomly missing levels φ in the systems that display wave chaos.

The missing level statistics and the analysis of the power spectrum of level fluctuations were also investigated for the three-dimensional chaotic microwave cavity. Also, in this case the experimental results are in good agreement with the analytical expressions dependent on the parameter φ . However, this theoretical approach applied to a problem of incomplete spectra with many unresolved states may fail. In this case the calculations based on the random matrix theory can be useful for the determination of the fraction of observed levels.

Summarizing, I may conclude that both the elastic enhancement factor and the power spectrum can be used as very useful tools for the investigation of the properties of low-dimensional wave structures that simulate quantum systems. In addition, they were successfully applied in three-dimensional wave structures. The above measures together with the short- and long- range spectral correlators can provide a valuable information about the studied systems, including their symmetry and chaoticity, in the conditions that include strong absorption and missing levels. The studies of real physical systems may greatly benefit from them.

BIBLIOGRAPHY

- [1] L. A. Safonov, E. Tomer, V. V. Strygin, Y. Ashkenazy, and S. Havlin, *Chaos: An Interdisciplinary Journal of Nonlinear Science* **12**, 1006 (2002).
- [2] C. Kyrtsov and W. Labys, *Journal of Macroeconomics* **28**, 1 (2006).
- [3] A. Hubler and K. Phelps, *Complexity* **13**, 2 (2007).
- [4] O. Hul, M. Ławniczak, S. Bauch, A. Sawicki, M. Kuś, and L. Sirko, *Phys. Rev. Lett.* **109**, 040402 (2012).
- [5] A. N. Kolmogorov, *Lect Notes Physics* **93**, 51 (1979).
- [6] E. N. Lorenz, *AMSJ* **20**, 130 (1963).
- [7] T. Y. Li and J. A. Yorke, *American Mathematical Monthly* **82**, 985 (1975).
- [8] "The Chaos hypertextbook," 2017. [Online]. Available: <https://hypertextbook.com/chaos/lyapunov-1/>.
- [9] F. Haake, *Quantum signatures of chaos* (Springer-Verlag, Germany, 1992).
- [10] M. L. Mehta, *Random Matrices and the Statistical Theory of Energy Levels* (Academic Press, London, 1990).
- [11] T. Guhr, A. Muller-Groeling, and H. A. Wiedemuller, *Phys. Rep.* **299**, 189 (1998).
- [12] M. Ławniczak, PhD thesis (2011).
- [13] M. V. Berry and M. Tabor, *Proc. R Soc.* **235**, 375394 (1977).
- [14] Ashraf A. Abul-Magd and Adel Y. Abul-Magd, arXiv:1311.2419 (2013).
- [15] B. Ratajska-Gadomska and W. Gadomski, *Optic Express* **17**, 14168 (2009).
- [16] T. M. Kardas, W. Gadomski, B. Ratajska-Gadomska, and P. Wasylczyk, *Optic Express* **18**, 26989 (2010).
- [17] H. -J. Stöckmann, *Chaos in Microwave Resonators* (Séminaire Poincaré IX, Marburg, 2006).

- [18] O. Hul, S. Bauch, P. Pakoński, N. Savytsky, K. Życzkowski, and L. Sirko, *Phys. Rev. E*, **69**, 056205 (2004).
- [19] M. Ławniczak, S. Bauch, O. Hul, and L. Sirko, *Phys. Rev. E* **81**, 046204 (2010).
- [20] H. -J. Stöckmann, *Quantum Chaos: An Introduction* (Cambridge University Press, Cambridge, 2000).
- [21] A. Richter and B. Dietz, *Chaos* **25**, 097601 (2015).
- [22] L. Pauling, *J. Chem. Phys.* **4**, 673 (1936).
- [23] J. A. Sanchez-Gil, V. Freilikher, I. Yurkevich, and A. A. Maradudin, *Phys. Rev. Lett.* **80**, 948 (1998).
- [24] R. Mittra and S. W. Lee, *Analytical Techniques in the Theory of Guided Waves* (Macmillan, 1971).
- [25] D. Kowal, U. Sivan, O. Entin-Wohlman, and Y. Imry, *Phys. Rev. B*, **42**, 9009 (1990).
- [26] Y. Imry, *Introduction to Mesoscopic Systems* (Oxford, New York, 1996).
- [27] T. Kottos and U. Smilansky, *Phys. Rev. Lett.* **79**, 4794 (1997).
- [28] P. Pakoński, K. Życzkowski, and M. Kuś, *J. Phys. A* **34**, 9303 (2001).
- [29] M. Ławniczak, A. Sawicki, S. Bauch, M. Kuś, and L. Sirko, *Phys. Rev. E* **89**, 032911 (2014).
- [30] T. Kottos and U. Smilansky, *Annals of Physics* **274**, 76124 (1999).
- [31] G. Berkolaiko, arXiv:1603.07356v2 (2016).
- [32] L. D. Landau and E. M. Lifshitz, *Electrodynamics of Continuous Media* (Pergamon Press, Oxford, 1960).
- [33] O. Hul and L. Sirko, *Phys. Rev. E* **83**, 066204 (2011).
- [34] M. Białous, V. Yunko, S. Bauch, M. Ławniczak, B. Dietz, and L. Sirko, *Phys. Rev. Lett.* **117**, 144101 (2016).
- [35] M. J. Giannoni, A. Voros, and J. Zinn Justin, *Chaos and Quantum Physics* (North-Holland, N.Y., 1991).

- [36] E. Faleiro, U. Kuhl, R. A. Molina, L. Muñoz, A. Relaño and J. Retamosa, Phys. Lett. A **358**, 251 (2006).
- [37] Y. Sinai, Notices of the AMS **51**, 412413 (2004).
- [38] H. -J. Stöckmann and J. Stein, Phys. Rev. Lett. **64**, 2215 (1990).
- [39] S. Sridhar, Phys. Rev. Lett. **67**, 785 (1991).
- [40] H. -D. Gräf, H. L. Harney, H. Lengers, C. H. Lewenkopf, C. Rangacharyulu, A. Richter, P. Schardt, and H. A. Weidenmüller, Phys. Rev. Lett. **69**, 1296 (1992).
- [41] L. Sirko, P. M. Koch, and R. Blümel, Phys. Rev. Lett. **78**, 2940 (1997).
- [42] R. Blümel, P. M. Koch, and L. Sirko, Foundations of Physics **31**, 269 (2001).
- [43] Y. Hlushchuk, L. Sirko, U. Kuhl, M. Barth, and H. -J. Stöckmann, Phys. Rev. E, **63**, 046208 (2001).
- [44] E. Hurt, *Quantum chaos and mesoscopic systems* (Springer, 1997).
- [45] O. Bohigas and M. P. Pato, Phys. Lett. B **595**, 171 (2004).
- [46] D. Ullmo, *The Bohigas-Giannoni-Schmit conjecture* (Orsay cedex, 2016).
- [47] B. B. Mandelbrot, *Multifractals and 1/f Noise* (Springer, 1963–1976).
- [48] J. M. G. Gómez, A. Relaño, J. Retamosa, E. Faleiro, L. Salasnich, M. Vranicar, and M. Robnik, Phys. Rev. Lett. **94**, 084101 (2005).
- [49] A. Relaño, J. M. G. Gómez, R. A. Molina, J. Retamosa, and E. Faleiro, Phys. Rev. Lett. **89**, 244102 (2002).
- [50] E. Faleiro, J. M. G. Gómez, R. A. Molina, L. Munoz, A. Relaño, and J. Retamosa, Phys. Rev. Lett. **93**, 244101 (2004).
- [51] P. A. Moldauer, Phys. Rev. **123**, 968 (1961).
- [52] Y. Kharkov and V. Sokolov, Phys. Lett. B **718**, 1562 (2013).
- [53] Y. V. Fyodorov, D. V. Savin, and H. -J. Sommers, J. Phys. A **38**, 10731 (2005).
- [54] D. V. Savin, Y. V. Fyodorov, and H. -J. Sommers, Acta Phys. Pol. A **109**, 53 (2006).
- [55] W. Kretschmer and M. Wangler, Phys. Rev. Lett. **41**, 1224 (1978).

- [56] J. J. M. Verbaarschot, *Ann. Phys.* **168**, 368 (1986).
- [57] C. Fiachetti and B. Michielsen, *Electron. Lett.* **39**, 1713 (2003).
- [58] X. Zheng, S. Hemmady, T. M. Antonsen Jr., S. M. Anlage, and E. Ott, *Phys. Rev. E* **73**, 046208 (2006).
- [59] J. -H. Yeh, Z. Drikas, J. Gil, S. Hong, B. T. Taddese, E. Ott, T. M. Antonsen, T. Andreadis, and S. M. Anlage, *Acta Phys. Pol. A* **124**, 1045 (2013).
- [60] B. Dietz, T. Friedrich, H. L. Harney, M. Miski-Oglu, A. Richter, F. Schafer and H. A. Weidenmüller, *Phys. Rev. E* **81**, 036205 (2010).
- [61] M. Ławniczak, S. Bauch, O. Hul, and L. Sirko, *Phys. Scr.* **T143**, 014014 (2011).
- [62] M. Ławniczak, S. Bauch, O. Hul, and L. Sirko, *Phys. Scr.* **T147**, 014018 (2012).
- [63] B. Michielsen, F. Isaac, I. Junqua, and C. Fiachetti, *arXiv:math-ph/0702041* (2007).
- [64] V. V. Sokolov and O. V. Zhirov, *Phys. Rev. E* **91**, 052917 (2015).
- [65] U. Stoffregen, J. Stein, H. -J. Stöckmann, M. Kuś, and F. Haake, *Phys. Rev. Lett.* **74**, 2666 (1995).
- [66] R. A. Molina, J. Retamosa, L. Muñoz, A. Relaño, and E. Faleiro, *Phys. Lett. B* **644**, 25 (2007).
- [67] M. Robnik and G. Veble, *J. Phys. A* **31**, 4669 (1998).
- [68] F. Leyvraz, J. Quezada, T. H. Seligman, and M. Lombardi, *Phys. Rev. Lett.* **67**, 2921 (1991).
- [69] S. Hemmady, X. Zheng, J. Hart, T. M. Antonsen, E. Ott i S. M. Anlage, *Phys. Rev. E* **74**, 036213 (2006).
- [70] M. Ławniczak, O. Hul, S. Bauch, P. Šeba, and L. Sirko, *Phys. Rev. E* **77**, 056210 (2008).
- [71] D.V. Savin, H. -J. Sommers, and Y. V. Fyodorov, *JETP Lett.* **82**, 544 (2005).
- [72] P. Šeba, *Phys. Rev. Lett.* **64**, 1855 (1990).
- [73] T. Tudorovskiy, U. Kuhl, and H. -J. Stöckmann, *New J. Phys.* **12**, 123021 (2010).
- [74] K. M. Frahm and D. L. Shepelyansky, *Phys. Rev. Lett.* **79**, 1833 (1997).

- [75] N. Savytsky, O. Hul, and L. Sirko, Phys. Rev. E **70**, 056209 (2004).
- [76] R. A. Molina, L. Muñoz, A. Relaño, and E. Faleiro, Phys. Lett. B **644**, 25 (2007).
- [77] B. Dietz, T. Friedrich, H. L. Harney, M. Miski-Oglu, A. Richter, F. Schäfer, J. Verbaarschot, and H. A. Weidenmüller, Phys. Rev. Lett. **103**, 064101 (2009).
- [78] M. Allgaier, S. Gehler, S. Barkhofen, H. -J. Stöckmann, and U. Kuhl, Phys. Rev. E **89**, 022925 (2014).
- [79] D. S. Jones, *Theory of Electromagnetism* (Pergamon Press, Oxford, 1964).
- [80] N. Savytsky, A. Kohler, S. Bauch, R. Blümel, and L. Sirko, Phys. Rev. E **64**, 036211 (2001).
- [81] M. S. Santhanam and J. N. Bandyopadhyay, Phys. Rev. Lett. **95**, 114101 (2005).
- [82] A. Relaño, Phys. Rev. Lett. **100**, 224101 (2008).
- [83] B. Dietz, V. Yunko, M. Białous, S. Bauch, M. Ławniczak, and L. Sirko, Phys. Rev. E **95**, 052202 (2017).
- [84] A. Frish, M. Mark, K. Aikawa, F. Ferlaino, J. Bohn, C. Makrides, A. Perov, and S. Kotochigova, Nature **507**, 475 (2014).
- [85] J. Mur-Petit and R. A. Molina, Phys. Rev. E **92**, 042906 (2015).
- [86] H. I. Liou, H. S. Camarda, and F. Rahn, Phys. Rev. C **5**, 131 (1972).
- [87] T. Zimmermann, H. Köppel, L. S. Cederbaum, G. Persch, and W. Demtröder, Phys. Rev. Lett. **61**, 3 (1988).
- [88] H. Alt, H. -D. Gräf, H. L. Harney, R. Hofferbert, H. Lengeler, A. Richter, P. Schardt, and H. A. Weidenmüller, Phys. Rev. Lett. **74**, 62 (1995).
- [89] P. So, S. M. Anlage, E. Ott, and R. N. Oerter, Phys. Rev. Lett. **74**, 2662 (1995).
- [90] S. Hemmady, X. Zheng, E. Ott, T. M. Antonsen, and S. M. Anlage, Phys. Rev. Lett. **94**, 014102 (2005).
- [91] B. Dietz and A. Richter, Chaos **25**, 097601 (2015).
- [92] S. Deus, P.M. Koch, and L. Sirko, Phys. Rev. E **52**, 1146 (1995).
- [93] R. L. Weaver, Acoust. Soc. Am. **85**, 1005 (1989).

- [94] C. Ellegaard, T. Guhr, K. Lindemann, J. Nygard, and M. Oxborrow, *Phys. Rev. Lett.* **77**, 4918 (1996).
- [95] H. Alt, C. Dembowski, H. -D. Gräf, R. Hofferbert, H. Rehfeld, A. Richter, R. Schuhmann, and T. Weiland, *Phys. Rev. Lett.* **79**, 1026 (1997).
- [96] M. Ławniczak, M. Białous, V. Yunko, S. Bauch, and L. Sirko, *Phys. Rev. E* **98**, 012206 (2018).
- [97] V. Yunko, M. Białous, S. Bauch, M. Ławniczak, and L. Sirko, The 11th CHAOS 2018 International Conference (2018), to be printed.
- [98] O. Bohigas, M. J. Giannoni, and C. Schmit, *Phys. Rev. Lett.* **52**, 1 (1984).
- [99] O. Bohigas, R. U. Haq, and A. Pandey, in *Nuclear Data for Science and Technology*, edited by K.H. Böckhoff (Reidel, Dordrecht, 1983).
- [100] M. Sieber, U. Smilansky, S. C. Creagh, and R. G. Littlejohn, *J. Phys. A* **26**, 6217 (1993).
- [101] B. Dietz, T. Guhr, B. Gutkin, M. Miski-Oglu, and A. Richter, *Phys. Rev. E* **90**, 022903 (2014).
- [102] M. Ławniczak, O. Hul, S. Bauch, and L. Sirko, *Acta Phys. Pol. A* **116**, 749 (2009).
- [103] J. -B. Gros, O. Legrand, F. Mortessagne, E. Richalot, and K. Selezmani, *Wave Motion* **51**, 664 (2014).
- [104] R. Balian and C. Bloch, *Ann. Phys.* **64**, 271 (1971).
- [105] H. P. Baltes, *Phys. Rev. A* **6**, 2252 (1972).
- [106] R. Balian and C. Bloch, *Ann. Phys.* **84**, 559 (1974).
- [107] M. Ławniczak, M. Białous, V. Yunko, S. Bauch, and L. Sirko, *Phys. Rev. E* **91**, 032925 (2015).